NTNU – Trondheim
Norwegian University of
Science and Technology

Simulations of impact using the modified Gurson model

Christian Dalheim Øien
Vegard Schønberg

Civil and Environmental Engineering
Submission date: June 2012
Supervisor: Jon Andreas Støvneng, IFY
Co-supervisor: Odd-Sture Hopperstad, SIMLab/Institutt for Konstruksjonsteknikk ved Fakultet for Ingeniørvitenskap og Teknologi

Norwegian University of Science and Technology
Department of Physics

Department of Structural Engineering
Faculty of Engineering Science and Technology
NTNU – Norwegian University of Science and Technology

MASTER'S THESIS 2012
for
Vegard Schønberg and Christian Dalheim Øien

Simulations of impact using the modified Gurson model

The effect of target strength on the perforation resistance of plates has previously been studied at SIMLab using three different structural steels (Weldox 460E, Weldox 700E and Weldox 900E). The effects of strain hardening, strain rate hardening, temperature softening and stress triaxiality on the material strength and ductility were determined for the steels by conducting tensile and dynamic tests over a wide range of strain rates and temperatures. The test data were used to determine material constants in modified versions of the Johnson-Cook constitutive relation and fracture criterion. Perforation tests were then carried out in a compressed gas gun on 12 mm thick plates with blunt, conical and ogival nosed projectiles. The experimental results indicated that for impacts with blunt projectiles the ballistic limit velocity decreased for increasing strength, while the opposite was found in tests with conical and ogival projectiles. FE simulations using LS-DYNA revealed that the numerical code is able to describe the physical mechanisms in the perforation events with reasonable accuracy, but the experimental trend of a decrease in ballistic limit with an increase in target strength for blunt projectiles was not obtained. The main objective in this project is to re-simulate these experimental tests using the modified Gurson model to see if better agreement with the experimental results can be achieved using this model.
The main topics in the research project will be as follows:

- Literature review: A state-of-the-art on the impact of steel plates with special emphasis on dynamic fracture should be conducted.

- Material tests: Shear and plane strain tension tests on Weldox 460E, Weldox 700E and Weldox 900E should be conducted using DIC/DIT to extract the required data.

- Calibration: Based on the available experimental data the modified Gurson model should be calibrated and validated for the various steel alloys.

- Numerical simulations: Using the modified Gurson model, numerical simulations using LS-DYNA of the plate perforation tests should be carried out. Both adiabatic conditions and full heat transfer should be considered in the analysis.

- Reporting.

Supervisors: Odd Sture Hopperstad, Torodd Berstad and Tore Børvik (NTNU).

The thesis must be written according to current requirements and submitted to Department of Structural Engineering, NTNU, no later than June 15th, 2012.

NTNU, January 16th, 2012

Odd Sture Hopperstad
Professor

Preface

This thesis is written as the final part of the five year education of Christian Dalheim Øien and Vegard Schønberg achieving the degree *Master of Science*. The work was done under the supervision of prof. Odd Sture Hoppstad and prof. Tore Børvik at the Structural Impact Laboratory (SIMLAB)[1], Department of Structural Engineering, Norwegian University of Science and Technology (NTNU).

The work with the thesis has to a great extent involved work with finite element method (FEM) mechanics simulations using the finite element code LS–DYNA[2] and the pre- and post-processing software LS–PrePost freely availiable on the internet[3]. A 'user material sub-routine' (UMAT) implemented by Torodd Berstad[4] was used in order to use the studied material model (the modified Gurson model) with this code.

The work with this thesis was constituted of two main parts; first of all calibrating the modified Gurson model parameters for three different steel alloys, and then secondly using these calibrated material models to perform FEM simulations of impact between blunt projectiles and steel plates. Chapter 4 describes the work with adjusting the material parameters used in the material models, and must be said to have taken up about 90% of the time availiable to the authors regarding this thisis. Difficulties with the implementation of the modified Gurson model has also slowed our work down, but has on the other side made the implementation more robust. In chapter 5 we breifly describe impact exteriments done earlier by dr. Sumita Dey at SIMLab, and in chapter 6 we describe the set-ups and results regarding impact simulations that we have run. Chapter 2 gives a brief overview of the theory that our work is based on, and in chapters 7 and 8 we draw conclusions and propose further work to be done on the present field of study, respectively.

[1] www.ntnu.edu/web/simlab

[2] Livermore Software Technology Corporation, www.lstc.com/products/ls-dyna

[3] www.lstc.com/lspp

[4] Research scientist Torodd Berstad at SIMLab, Department of Structural Engineering, NTNU. E-mail: torodd.berstad@ntnu.no

Acknowledgments

Tanks to our supervisors prof. Odd Sture Hopperstad and prof. Tore Børvik for critical frequent support, critical guidance and. Thanks also to PhD candidates Gaute Gruben and Knut Gaarder Rakvåg, SIMLab, for valuable help with multiple details in sections 2.5 and 2.6.

We have greatly appreciated continuous help from Torodd Berstad regarding the finite element code LS–DYNA and use of the pre- and post-processor LS-PrePost, and for sharing and explaining the *Fortran* code implementing the modified Gurson model into LS–DYNA.

Thanks to post doc. Egil Fagerholt for performing setup and analysis necessary for the calculation of the DIC strain fields in used in chapter 6 and to Trond Auestad for performing the setup and execution of the shear stress tests and plain strain tests described in the same chapter.

Abstract

We have performed modified Gurson model calibrations to the steel alloys Weldox® 460E, Weldox® 700E and Weldox® 900E through finite element method (FEM) simulations of various tensile material tests performed, and used these material models to perform FEM simulations of impact of blunt tool steel projectiles on target plates made out of these steel alloys. The purpose of these FEM simulations was to study the dependence of target plate steel alloy on the ballistic limit velocity of the projectile resulting from the modified Gurson model. It was found that the modified Gurson model is able to reproduce the dependence seen in experiments, but that it is strongly dependent on a certain model parameter related to the shear stress dependence on material damage. We have also discovered potential problems, and possible solutions, regarding the calibration of these material models and the use of them in the FEM impact simulations carried out.

Sammendrag

Vi har utført kabrering av den modifiserte Gurson-modellen til stållegeringene Weldox® 460E, Weldox® 700E og Weldox® 900E gjennom simuleringer, ved bruk av elementmetoden (FEM), av forskjellige, utførte strekkprøver, og brukt disse materialmodellene til å simulere sammenstøt mellom flatnesede verktøystålprosjektiler og målplater av disse stållegeringene. Formålet med disse FEM-simuleringene var å studere avhengigheten av målplatestållegeringen på den ballistiske grensen til sammenstøtet som den modifiserte Gurson-modellen forutsier. Det ble funnet at den modifiserte Gurson-modellen er i stand til å reprodusere avhengigheten som observeres i eksperimenter, men at denne avhengigheten er sterkt avhengig av en spesifikk modellparameter som styrer avhengigheten av skjærspenninger på skaden påført materialet. Vi har også avdekket potensielle problemer, og mulige løsninger, vedrørende kalibreringen av disse materialmodellene og bruken av dem i de utførte FEM-simuleringene.

Vegard Schønberg Christian Dalheim Øien

Contents

Figures

Tables

Notation

$\dot{x}$	Time derivative $\frac{\mathrm{d}}{\mathrm{d}t}x$
δ_{ij}	Kronecker delta
λ_e, μ_e	Lame constants of elasticity
c_T	Specific heat capacity
ρ	Mass density
β_{ij}	Thermal stress coefficient tensor
β_{TQ}	Taylor-Quinney coefficient of adiabatic heating
θ_i, Q_i	Voce rule strain hardening parameters
C	Strain rate hardening parameter
m	Temperature softening parameter
σ_E	Engineering uniaxial stress
σ_t	True (or Cauchy) uniaxial stress
σ_b	Brigdman corrected uniaxial stress
σ_0	Yield stress
σ_{ij}	Cauchy stress tensor
s_{ij}	Deviatoric Cauchy stress tensor
σ_e	von Mises equivalent stress
σ_M	von Mises equivalent matrix stress
σ_m	Hydrostatic stress
σ^*	Stress triaxiality
L	Lode parameter
ϑ	Lode angle

I_1, I_2, I_3	Cauchy stress tensor invariants
J_2, J_3	Cauchy stress deviator tensor invariants
$\sigma_\mathrm{I}, \sigma_\mathrm{II}, \sigma_\mathrm{III}$	Principal Cauchy stresses
s_1, s_2, s_3	Principal deviatoric Cauchy stresses
ε_E	Engineering uniaxial strain
ε_l	Logarithmic (or true) uniaxial strain
ε_l^P	Logarithmic (or true) uniaxial plastic strain
ε_n	True uniaxial strain at necking
ε_{ij}	Strain tensor
ε_{ij}^P	Plastic strain tensor
ε_e	von Mises equivalent strain
ε_e^P	Plastic von Mises equivalent strain
ε_M^P	Plastic von Mises equivalent matrix strain
F	Yield function
$\dot{\lambda}$	Plastic multiplier
f	Void volume fraction
f_0	Initial void volume fraction
q_1, q_2	Tvergaard parameters of the Gurson model
k_ω	Extended Gurson model parameter
$\omega(\sigma_{ij})$	Extended Gurson model "omega" function

Einstein summation convention

$$a_{ij}b_{ij}\cdots = \sum_{i=1}^{3}\sum_{j=1}^{3} a_{ij}b_{ij}\cdots$$

Summation is applied over repeated indices (unless otherwise stated)

Chapter 1
Background and motivation

Penetration and perforation experiments with steel plates exposed to ballistic impact have been carried out and studied extensively over the recent years at at SIMLab[1] by, amongst others, Tore Børvik, Odd Sture Hopperstad, Torodd Berstad and Magnus Langseth. See e.g. [5], [6], [7], [8]. It has been desirable to study the smallest velocity in which target penetration is obtained, i.e. the *ballistic limit velocity*, and its the dependence on the target plate thickness, target plate hardness and projectile nose shape. The results have been attempted reproduced numerically using different material models and constitutive relations. Up until now the dependency of the target plate steel alloy on the ballistic limit velocity for blunt nodes projectiles have not been reproduced by FEM simulations. The main objective with this thesis is thus to see if this dependency can be reproduced for blunt nosed projectiles using the modified Gurson model. If that is the case, then the studied model is able to describe the differences in localization effects in materials of different strength in a better way than the model used earlier.

One motivation to now use the *modified* Gurson model in such studies is the modification of the original Gurson model, for including shear induced failure, made by Nahshon and Hutchinson in 2008 [26], since the shear stress dependence on the material damage introduced is likely to have a significant effect on the perforation process that the "plugging" of the plate is based on. Through such work the authors also intend to gain knowledge on how to calibrate the modified Gurson model properly and to document the experiences made.

[1] CRI Structural Impact Laboratory, see **??**

Chapter 2
Theory

2.1 Tension tests

We start out by explaining the basics of stress, strain and localization. In a tension test the nominal (or engineering) stress is given by

$$\sigma_E = \frac{N}{A_0} \tag{2.1}$$

where N is the tension force and A_0 is the initial cross-sectional area of the test specimen's parallel area. The corresponding strain is the nominal strain in the specimen, obtained by

$$\varepsilon_E = \frac{L - L_0}{L_0}. \tag{2.2}$$

The relations (2.1) and (2.2) are clearly valid for small deformations only, as they are based on the original dimensions of the specimen. For larger deformations, the decrease in cross-sectional area is significant and has to be accounted for. The infinitesimal strain due to an infinitesimal displacement u over a length L is, as in eq. (2.2),

$$\mathrm{d}\varepsilon_l = \frac{\mathrm{d}u}{L}$$

such that the *true* (or logarithmic) strain is given by

$$\begin{aligned} \varepsilon_l &= \int_0^{u_L} \frac{\mathrm{d}u}{L} = \int_{L_0}^{L} \frac{\mathrm{d}L'}{L'} \\ \varepsilon_l &= \ln \frac{L}{L_0} = \ln(\varepsilon_E + 1). \end{aligned} \tag{2.3}$$

This quantity includes the superimposed true elastic strain $\varepsilon_l^E = \sigma_t / E$ where E is the elastic modulus and σ_t is the true stress defined below. The true *plastic* strain is hence

$$\varepsilon_l^P = \varepsilon_l - \varepsilon_l^E = \varepsilon_l - \sigma_t / E. \tag{2.4}$$

Assuming plastic incompressibility and hence a constant volume of specimen's parallel area yields

$$A_0 L_0 = AL \Leftrightarrow A = A_0 \frac{L_0}{L}$$

such that the *true* (or Cauchy) stress, using eq. (2.3), is obtained as

$$\sigma_t = \frac{N}{A} = \frac{N}{A_0}\frac{L}{L_0} = \sigma_E \exp(\varepsilon_l)$$
$$\sigma_t = \sigma_E(\varepsilon_E + 1). \tag{2.5}$$

The equations (2.3) – (2.5) is valid for a finite, but uniform, deformation over the length of the specimen.

2.1.1 Necking

At some point during the straining of the test specimen the uniformness of the deformation discontinues as a localization is initiated somewhere along the specimen's parallel area. This implies that the force level reaches a critical value, since in this region the cross-sectional area will decrease rapidly along with increasing elongation — more rapid than the material hardens. This instability is called *diffuse necking* [13]. Differentiating the force N,

$$N = \sigma_t A \quad \Longrightarrow \quad \mathrm{d}N = \mathrm{d}\sigma_t A + \mathrm{d}A\sigma_t = 0,$$

dividing by $A\sigma_t$ and using the definition of true strain (2.3) gives

$$\frac{\mathrm{d}\sigma_t}{\sigma_t} = -\frac{\mathrm{d}A}{A} \overset{\text{pl.in.}}{=} \frac{\mathrm{d}L}{L} = \mathrm{d}\left(\ln\frac{L}{L_0}\right) \equiv \mathrm{d}\varepsilon_l, \tag{2.6}$$

noting the assumption of plastic incompressibility marked by 'pl. in.'. Thus diffuse necking occurs when

$$\frac{\mathrm{d}\sigma_t}{\mathrm{d}\varepsilon_l} = \sigma_t. \tag{2.7}$$

Since the deformation is localized after necking, true strain can no longer be calculated from force–displacement data along with the assumption of plastic incompressibility as in eq. (2.3) because of the deformation being concentrated somewhere in the gauge length of the specimen. For cylindrical specimens, however, the true strain can be fairly easily measured trough continuously measuring the smallest diameter of the specimen in the necked area, viz.

$$\varepsilon_l = \ln\frac{A_0}{A} = \ln\left[\frac{\pi/4}{\pi/4}\left(\frac{D_0}{D}\right)^2\right] = 2\ln\frac{D_0}{D}. \tag{2.8}$$

Thus, in order to have true-stress-true-strain measurements over the entire course of straining of the specimen — even after necking, the cross-sectional diameter must be measured during the test.

Influence on the magnitude of the uniaxial tension stress

As Dieter [13] effectively explains, *the formation of a neck in the tensile specimen introduces a complex triaxial state of stress in that region* [⋯] which *is in effect*

a mild notch. A notch under tension produces radial and transverse stresses which raise the value of longitudinal stress required to cause plastic flow. Therefore, the average true stress at the neck, which is determined by dividing the axial tensile load by the minimum cross-sectional area of the specimen at the neck, is higher than the stress $[\cdots]$ *required to cause flow if simple tension prevailed.*

A mathematical analysis, providing a correction to the average axial stress to compensate for the transverse stresses, was done by Bridgman in 1944 [4]. This analysis assumes a von Mises' yield criterion, that strains are constant over the cross section of the neck, and that both the arc of the neck and its cross section is circular. This Bridgman correction to the uniaxial stress is given by

$$\sigma_b = \frac{\sigma_t}{\left(1 + \frac{2R}{a}\right)\left(\ln\left[1 + \frac{a}{2R}\right]\right)}$$

where R is the neck radius and a is the radius of the cross section of the neck. This specific relation is not easy to use in practice, since a and R (especially) are hard to measure continuously. LeRoy et al. [23] proposed, based on empirical data, that the ratio a/R could be approximated by

$$a/R = a^* \equiv 1.1(\varepsilon_l^P - \varepsilon_n),$$

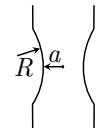

Fig. 2.1

where ε_n is the true uniaxial strain in the specimen when necking occurs and ε_l^P is the true plastic strain. In contrast to a and R, a^* is readily computed for each displacement point in a tension test data set resulting from force and extensometer displacement measurements only. In summary — this results in an empirical Bridgman correction that reads

$$\sigma_b = \frac{\sigma_t}{\left(1 + \frac{2}{a^*}\right)\frac{1}{2}\ln\left(1 + \frac{a^*}{2}\right)}. \tag{2.9}$$

2.2 Thermoviscoplasticity

The most basic assumption of plasticity models is the decomposition of the strain rate tensor into an elastic and a plastic part

$$\varepsilon_{ij} = \varepsilon_{ij}^e + \varepsilon_{ij}^p.$$

Thus the total strain of a material is constituted of a reversible and an irreversible part, the latter causing the material to flow plastically and dissipate energy. In viscoplasticity there are three base pillars in addition to this fundamental decomposition [10].

• The yield criterion $F(\sigma_{ij},\cdots) > 0$ where $F(\sigma_{ij},\cdots)$ is the yield function (or yield surface) which is a function of the stress state, i.e. the stress tensor σ_{ij}, and possibly other tensors and/or scalars (internal variables) as we will see later. When (and where) the criterion is satisfied the material flows plastically, i.e. it dissipates energy as it is strained and thus deforms irreversibly. The direction and magnitude in stress-strain-space of the plastic flow is governed by:

• The flow rule $\dot{\varepsilon}_{ij}^P = \dot{\lambda} h_{ij}$ determining the plastic strain rate tensor, assuring that the plastic dissipation is non-negative and specifying the magnitude and direction of plastic flow in stress-strain-space. Here $h_{ij} = \partial g / \partial \sigma_{ij}$ is the flow function defined by a plastic potential $g(\sigma_{ij},\cdots)$ and $\dot{\lambda} > 0$ is the plastic parameter. A *constitutive relation* is used to determine the plastic parameter, as e.g.

$$\dot{\lambda} = \begin{cases} 0 & , f < 0 \\ F(\sigma_{ij},\cdots)/\eta, & f > 0 \end{cases}, \tag{2.10}$$

which is the simplest possible choice [10], with η representing the resulting viscosity of the material. In general, it does does in general not need to be an explicitly defined relation as in eq. (2.10).

• The work-hardening rule $\sigma_e = \sigma_e(\varepsilon_e^P,\cdots)$ which specifies how some equivalent flow stress σ_e evolves during plastic flow. In thermoviscoplasticity it serves as a description of both the hardening due to increasing strain and strain rate and the material softening due to increasing temperature, in all three cases as a function of the respective variable. One common strain hardening rule is called the Voce law [33] and has the form

$$R = \sum_i Q_i \left(1 - \exp\left(-\frac{\theta_i}{Q_i}\varepsilon_l^P\right)\right), \tag{2.11}$$

introducing the material parameters σ_0, Q_i and θ_i (normally for $i = 1, 2$). This strain hardening expression could be combined, e.g. multiplicatively, with a strain rate hardening term on the form

$$\left(1 + \frac{\dot{\varepsilon}_e^P}{\dot{\varepsilon}_{e,0}^P}\right)^C,$$

and a temperature softening term on the form

$$1 - \left(\frac{T - T_0}{T_m - T_0}\right)^m,$$

introducing additional parameters C (rate dependence parameter), m (temperature dependence parameter), $\dot{\varepsilon}_{e,0}^P$ (reference strain rate) T_0 (reference temperature) and T_m (melting temperature).

2.3 Thermoelasticity

Assuming an isotropic material, and that temperature and strain variations are small enough to assure a linear behavior in those variables, the stress is given by [10]

$$\sigma_{ij} = \lambda_e \varepsilon_{mm} \delta_{ij} + 2\mu_e \varepsilon_{ij} - \beta \Delta T \delta_{ij}$$

where $\Delta T = T - T_0$ is the temperature variation, T_0 is the reference temperature, $\beta_{ij} = \beta \delta_{ij}$ is the 2^{nd} order tensor of thermal stress coefficients and λ_e and μ_e are the Lamé constants of elasticity. The inverse relation for the isotropic material reads [10]

$$\varepsilon_{ij} = -\frac{\nu}{E}\sigma_{kk}\delta_{ij} + \frac{1+\nu}{E}\sigma_{ij} + \alpha \Delta T \delta_{ij}$$

where $\alpha = \beta/3K$ is the linear coefficient of thermal expansion.

2.4 The modified Gurson model

The extended Gurson model (cf. Nahshon and Hutchinson [26] with proposed modification of the model presented by Gurson in 1977 [20]) is a model of porous plasticity, i.e. it is based on the assumption that the material to be described is a porous media with a void volume fraction f such that a part fV of its total volume V is made out of voids. In this thesis the voided material itself is modeled as thermoelastic-thermoviscoplastic.

Yield function

The model utilizes a yield function (or yield surface) on the form

$$F(\sigma_e, \sigma_m, f) = \left(\frac{\sigma_e}{\sigma_M}\right)^2 + 2q_1 f \cosh\left(\frac{3q_2}{2}\frac{\sigma_m}{\sigma_M}\right) - 1 - (q_1 f)^2 \tag{2.12}$$

where q_1 and q_2 are fitting parameters proposed by Tvergaard [32] and commonly set to $q_1 = 3/2$ and $q_2 = 1$. Furthermore the equivalent *macroscopic* stress $\sigma_e = \sqrt{3J_2} = \sqrt{\frac{3}{2}s_{ij}s_{ij}}$ where $s_{ij} = \sigma_{ij} - \frac{1}{3}\sigma_{kk}\delta_{ij}$ is the stress deviator and δ_{ij} is the Kronecker delta. This macroscopic equivalent stress is potentially degraded as a result of the growing void volume fraction f (cf. figure 2.7), while the equivalent *microscopic* stress σ_M is the strength of the unvoided matrix material which should be model led to harden monotonically with the equivalent plastic strain of the matrix material. Finally $\sigma_m = \frac{1}{3}\sigma_{kk}$ is the macroscopic mean (or hydrostatic) stress.

Void growth rate

The model is further incorporated through the void growth rate expressed as

$$\dot{f} = (1-f)\dot{\varepsilon}^P_{kk} + f k_\omega \omega(\sigma_{ij}) \frac{s_{ij}\dot{\varepsilon}^P_{ij}}{\sigma_e}. \tag{2.13}$$

Here $\dot{\varepsilon}_{ij}^P$ is the plastic strain rate tensor, k_ω is the third and final void growth parameter (in addition to $q_1$and q_2) and

$$\omega(\sigma_{ij}) = 1 - \frac{27J_3^2}{4J_2^3} = 1 - \left(\frac{27J_3}{2\sigma_e^3}\right)^2 \tag{2.14}$$

is a dimensionless function of the deviatoric stress tensor invariants. Details about this function follow in section 2.5 on page 9.

The first term in eq. (2.13) expresses the void growth rate due to volumetric straining while the second term accounts for weakening due to shearing of the voids. This second term constitutes the aforementioned modification of the model proposed by Nahshon and Hutchinson [26] and it is thus when $k_\omega \neq 0$ that one refers to the model as the *modified Gurson model*. One should note in the case of $k_\omega \neq 0$ that f is not longer an actual void fraction, but a damage variable that accounts for weakening due to both void growth and *void distortion*. In some cases there is also a third term on the right hand side of eq. (2.13) that accounts for nucleation of new voids on inclusions and particles. Here, however, void growth from the initial fraction f_0 of voids is assumed to be the only source of degradation of the material.

Flow rule

The flow rule applied in the work with this thesis is the *associated* flow rule

$$\dot{\varepsilon}_{ij}^P = \dot{\lambda}\frac{\partial F}{\partial \sigma_{ij}}, \tag{2.15}$$

which means that the plastic potential is taken as the yield function F itself. The flow rule is said to be *associated* since it is described by the same function as the one describing the onset of plastic yielding. Since the flow is proportional to the yield surface gradient $\partial F/\partial\sigma_{ij}$ it is orthogonal to the yield surface in strain-space.

Constitutive relation

In the (extended) Gurson model there is no explicit constitutive relation determining the plastic parameter through plastic flow increments. Instead, the present expression for work hardening $\sigma_M = \sigma_M(\varepsilon_M^P)$ is inserted in the expression for the yield function (2.12) such that $F = F(\sigma_{ij}, f, \sigma_M) \longrightarrow F(\sigma_{ij}, f, \varepsilon_M^P)$. Now, an implicit relation for ε_e^P (which is solved numerically in the work with this thesis) is obtained by equating the yield function to zero [21]. This is how the equivalent (microscopic) plastic strain rate $\dot{\varepsilon}_M^P$ is determined in each time step. The plastic parameter $\dot{\lambda}$ is then calculated using power conjugacy and the flow rule (2.15), viz.

$$\begin{aligned} \sigma_{ij}\dot{\varepsilon}_{ij}^P &= \sigma_{ij}\frac{\partial F}{\partial \sigma_{ij}} = (1-f)\sigma_M\dot{\varepsilon}_M^P \\ \Longrightarrow \dot{\lambda} &= \dot{\varepsilon}_M^P\frac{(1-f)\sigma_M}{\sigma_{ij}\dfrac{\partial F}{\partial \sigma_{ij}}}. \end{aligned}$$

Adiabatic heating

In penetration and perforation simulations *adiabatic heating* is necessary to describe damage initiation in the target plate arising at the perimeter of the projectile impact zone – or the *shear zone* – rapidly after contact. If one could do FEM simulations of penetration with grain scale elements one would probably [9] recover sparse tensional and shear strains damaging the target plate in the shear zone, and hence recover the start of the perforation process. But since in a given simulation the width of this shear zone will be is limited to the element size one must utilize a critical temperature element erosion criterion to describe it. Assuming adiabatic conditions the rise in temperature in a given element is here calculated as

$$\dot{T} = \beta_{TQ} \frac{\sigma_{ij} \dot{\varepsilon}^P_{ij}}{\rho c_T},$$

and the corresponding heat is assumed to stay in that element. Here $\beta_{TQ} \in \{0, 1\}$ is the Taylor-Quinney coefficient defining the fraction of the plastic work that leads to heating, ρ is the mass density and c_T is the specific heat capacity.

2.5 The function $\omega(\sigma_{ij})$

The function $\omega(\sigma_{ij})$ defined in equation (2.14), and involved in the second term in the expression for void growth (2.13), should be looked at more closely in order to reveal its central role in the modified Gurson model. This is done by first assuming axisymmetric and plane stress states, respectively, to express ω in terms of the *stress triaxiality* σ^*, defined as the ratio between hydrostatic and von Mises stress, and secondly by introducing the *Lode parameter* [24] to describe its dependencies in a general stress state.

2.5.1 Plane and axisymmetric stress states

Let us look at the *third deviatoric stress invariant* J_3, contained in eq. (2.14), given by

$$J_3 = s_{ij} s_{ik} s_{jk} = (\sigma_{\mathrm{I}} - \sigma_m)(\sigma_{\mathrm{II}} - \sigma_m)(\sigma_{\mathrm{III}} - \sigma_m)$$

where $\sigma_{\mathrm{I}}, \sigma_{\mathrm{II}}, \sigma_{\mathrm{III}}$ are the principal stresses. Let us assume a *plane stress* state, such that $\sigma_{\mathrm{II}} = 0$. By inserting $\sigma_m = \sigma_{kk}/3 = (\sigma_{\mathrm{I}} + \sigma_{\mathrm{III}})/3$ we find that

Assuming plane stress

$$J_3 = \frac{2}{27}\sigma_{\mathrm{I}}^3 - \frac{1}{9}\sigma_{\mathrm{I}}^2\sigma_{\mathrm{III}} - \frac{1}{9}\sigma_{\mathrm{I}}\sigma_{\mathrm{III}}^2 + \frac{2}{27}\sigma_{\mathrm{III}}^3.$$

Expressing both σ_{I} and σ_{III} by σ_e and σ^* will therefore suffice in doing the same with $\omega(\sigma_{ij})$, which is the intention of this section. For σ_{III} we simply use that

$\sigma_m = (\sigma_\mathrm{I} + \sigma_\mathrm{III})/3$ such that

$$\begin{aligned}\sigma_\mathrm{III} &= 3\sigma_m - \sigma_\mathrm{I} \\ &= 3\sigma_e\sigma^* - \sigma_\mathrm{I}. \end{aligned} \tag{2.16}$$

To express σ_I by σ_e and σ^* we look at the *second deviatoric stress invariant* J_2 given by

$$\begin{aligned} J_2 &= \frac{1}{2}s_{ij}s_{ij} = \frac{1}{2}(\sigma_{ij} - \frac{1}{3}\sigma_{kk}\delta_{ij})(\sigma_{ij} - \frac{1}{3}\sigma_{kk}\delta_{ij}) \\ &= \frac{1}{2}\sigma_{ij}\sigma_{ij} - \frac{1}{6}\sigma_{kk}^2 = \frac{1}{2}(\sigma_\mathrm{I}^2 + \sigma_\mathrm{III}^2) - \frac{1}{6}(\sigma_\mathrm{I} + \sigma_\mathrm{III})^2 \\ &= \frac{1}{3}(\sigma_\mathrm{I}^2 - \sigma_\mathrm{I}\sigma_\mathrm{III} + \sigma_\mathrm{III}^2) = \frac{1}{3}(\sigma_\mathrm{I}^2 - \sigma_\mathrm{I}[3\sigma_e\sigma^* - \sigma_\mathrm{I}] + [3\sigma_e\sigma^* - \sigma_\mathrm{I}]^2) \\ &= \sigma_\mathrm{I}^2 - 3\sigma_\mathrm{I}\sigma_e\sigma^* + 3(\sigma_e\sigma^*)^2. \end{aligned}$$

Since we also have, by definition, that $J_2 \equiv \sigma_e^2/3$ we see that σ_I is given by the (smallest) root of the second order equation

$$\sigma_\mathrm{I}^2 - 3\sigma_e\sigma^*\sigma_\mathrm{I} + 3\sigma_e^2(\sigma^*)^2 - \frac{1}{3}\sigma_e^2 = 0,$$

i.e.

$$\sigma_\mathrm{I} = \sigma_e\left(\frac{3}{2}\sigma^* - \sqrt{\frac{1}{3} - \frac{3}{4}(\sigma^*)^2}\right) \in \mathbb{R} \text{ if } -\frac{2}{3} < \sigma^* < \frac{2}{3}. \tag{2.17}$$

By looking at eqs. (2.16) and (2.17) we see that σ_e is cyclic in the function ω, such that

$$\omega = \omega(\sigma^*) = 1 - \left(\frac{2\sigma_\mathrm{I}^3 - 3\sigma_\mathrm{I}^2\sigma_\mathrm{III} - 3\sigma_\mathrm{I}\sigma_\mathrm{III}^2 + 2\sigma_\mathrm{III}^3}{2\sigma_e^3}\right)^2 \tag{2.18}$$

is a function of σ^* only. This can be seen clearly [19] by inserting eq. (2.17) into eq. (2.16) to obtain

$$\sigma_\mathrm{III} = \sigma_e\left(\frac{3}{2}\sigma^* + \sqrt{\frac{1}{3} - \frac{3}{4}(\sigma^*)^2}\right) \tag{2.19}$$

and further inserting this into eq. (2.18), which, still remembering the assumption of plane stress, yields the explicit expression

$$\begin{aligned}\omega = \omega(\sigma^*) &= 1 - \frac{81}{4}\left((\sigma^*)^2 - 6(\sigma^*)^4 + 9(\sigma^*)^6\right) \\ &= 1 - \left(\frac{9}{2}\sigma^*\left(3(\sigma^*)^2 - 1\right)\right)^2 \end{aligned} \tag{2.20}$$

Now, instead of assuming plane stress, let us assume the stress state to be *axisymmetric* , i.e. $\sigma_{\mathrm{I}} \geq \sigma_{\mathrm{II}} = \sigma_{\mathrm{III}}$ or $\sigma_{\mathrm{I}} = \sigma_{\mathrm{II}} \geq \sigma_{\mathrm{III}}$. Then

ASSUMING AXISYM-METRIC STRESS

$$\begin{aligned} J_3 &= (\sigma_{\mathrm{I}} - \sigma_m)(\sigma_{\mathrm{II}} - \sigma_m)(\sigma_{\mathrm{III}} - \sigma_m) \\ &= \pm\frac{2}{27}(\sigma_{\mathrm{I}} - \sigma_{\mathrm{III}})^3 \\ &= \pm\frac{2}{27}\sigma_e^3 \end{aligned}$$

such that

$$\omega(\sigma_{ij}) = 1 - \left(\frac{27J_3}{2\sigma_e^3}\right)^2 = 1 - 1 = 0.$$

In summary we then have for the function ω that

$$\omega(\sigma^*) = \begin{cases} 1 - \left(\frac{9}{2}\sigma^*\left(3(\sigma^*)^2 - 1\right)\right)^2 & \text{, plane stress} \\ 0 & \text{, axisymmetric stress} \end{cases} \tag{2.21}$$

As in the 2008 paper by Nahshon and Hutchinson [26] proposing the modification to the original Gurson model, one could assume plane stress for shear stress modes, $|\sigma^*| < 1/3$, and axisymmetric stress for all cases of $\sigma^* \geq 1/3$. Then the function $\omega(\sigma^*)$ as defined by eq. (2.21) is as curve (a) plotted in figure 2.2. For plane stress in general the function is as given by curve (b) in the same figure and takes on real values in the interval $-2/3 < \sigma^* < 2/3$.

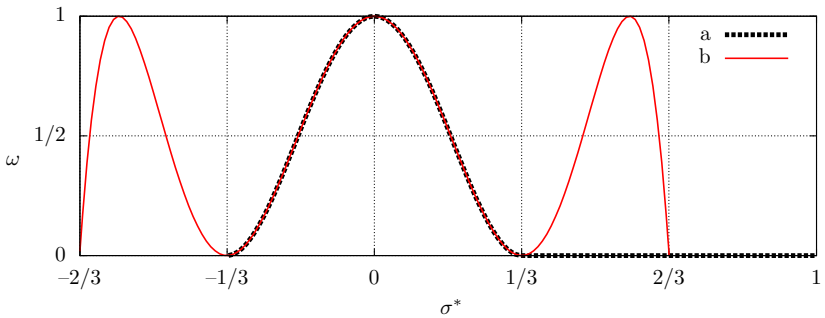

Fig. 2.2: The function $\omega = \omega(\sigma^*)$ (a) given the assumptions of plane stress for $|\sigma^*| < 1/3$ and axisymmetric stress for $\sigma^* \geq 1/3$, i.e. as given by eq. (2.21), and (b) for plane stress in general, i.e. as given by eq. (2.18).

We see from this figure and the void growth assumption in the modified Gurson model, eq. (2.13), that for plane and axisymmetric stress states $\omega(\sigma^*)$ adds a contribution to the void growth for stress triaxialities $|\sigma^*| < 1/3$. This means that the modified Gurson model adds void growth in compressional and tensional shear

stress states to the original model, making the modeled material more brittle in tensional shear stress than if the original Gurson model is used, and making sure it has brittleness *at all* in pure and compressional shear stress states. The size of this contribution is evidently controlled by the only parameter introduced in the extension of the Gurson model — k_ω.

2.5.2 General stress states

In a general stress state, i.e. without the assumptions stated above of plane and axisymmetric stress in different triaxiality intervals, we need to utilize the *Lode parameter* [24] to describe the function ω. It is defined as[1]

$$L = \frac{2\sigma_{\mathrm{II}} - \sigma_{\mathrm{I}} - \sigma_{\mathrm{III}}}{\sigma_{\mathrm{I}} - \sigma_{\mathrm{III}}}. \tag{2.22}$$

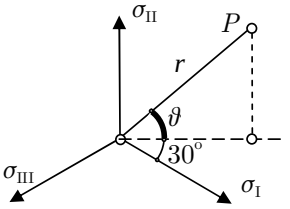

Fig. 2.3: Graphic representation of the Lode angle ϑ in the deviatoric plane

Further the *Lode angle* of a stress state $P(\sigma_{\mathrm{I}}, \sigma_{\mathrm{II}}, \sigma_{\mathrm{III}})$ is defined as the angle ϑ in the deviatoric plane in Haigh–Westergaard space that separates (the projection of) the first principal direction and the vector from the origin to P minus 30°, as shown in figure 2.3. It can then be shown that

$$L = -\sqrt{3}\tan(\vartheta). \tag{2.23}$$

The Lode parameter thus describes the deviatoric part of a general stress state. Also note that assuming ordered principal strains one has $-\pi/6 < \vartheta < \pi/6$ and $-1 < L < 1$.

Let us now express the third deviatoric stress invariant J_3 by L. It can be shown by geometric considerations [21] that the deviatoric stresses in Haigh–Westergaard space can be expressed in terms of the Lode angle ϑ as

$$\begin{aligned} s_1 &= \sigma_{\mathrm{I}} - \sigma_m = \frac{1}{3}\sigma_e\left(\sqrt{3}\cos\vartheta - \sin\vartheta\right) \\ s_2 &= \sigma_{\mathrm{II}} - \sigma_m = \frac{2}{3}\sigma_e \sin\vartheta \\ s_3 &= \sigma_{\mathrm{III}} - \sigma_m = \frac{1}{3}\sigma_e\left(\sqrt{3}\cos\vartheta + \sin\vartheta\right) \end{aligned} \tag{2.24}$$

where $\sigma_e = \sqrt{3J_2} = \sqrt{\frac{3}{2}s_{ij}s_{ij}}$ as mentioned earlier. Now using $J_3 = s_1 s_2 s_3$ and the trigonometric relation

$$\sin x(3\cos^2 x - \sin^2 x) = \sin(3x)$$

[1] Note that definitions of the Lode parameter with the opposite sign does appear in literature.

we arrive at

$$\begin{aligned} J_3 &= \frac{2}{27}\sigma_e^3 \left(\sqrt{3}\cos\vartheta - \sin\vartheta\right) \sin\vartheta \left(\sqrt{3}\cos\vartheta + \sin\vartheta\right) \\ &= \frac{2}{27}\sigma_e^3 \sin\vartheta \left(3\cos^2\vartheta - \sin^2\vartheta\right) \\ &= \frac{2}{27}\sigma_e^3 \sin(3\vartheta). \end{aligned} \tag{2.25}$$

Using yet another trigonometric relation, namely

$$\sin(3\arctan x) = \frac{3x - x^3}{(1+x^2)^{3/2}},$$

it is readily shown [19], rearranging eq. (2.25) and using eq. (2.23), that

$$\begin{aligned} \frac{27J_3}{2\sigma_e^3} &= \sin(3\vartheta) = \sin\left(3\arctan(-L/\sqrt{3})\right) \\ &= \frac{3L - \frac{1}{3}L^3}{\sqrt{3}\left(\frac{1}{3}L^2+1\right)^{3/2}} = \frac{\sqrt{3}\left(9L - L^3\right)}{9\left(\frac{1}{3}L^2+1\right)^{3/2}} \end{aligned}$$

such that we can finally arrive at

$$\begin{aligned} \omega(\sigma_{ij}) &\equiv 1 - \left(\frac{27J_3}{2\sigma_e^3}\right)^2 \\ &= \boxed{\omega(L) = 1 - \frac{\left(9L - L^3\right)^2}{\left(L^2+3\right)^3}}. \end{aligned} \tag{2.26}$$

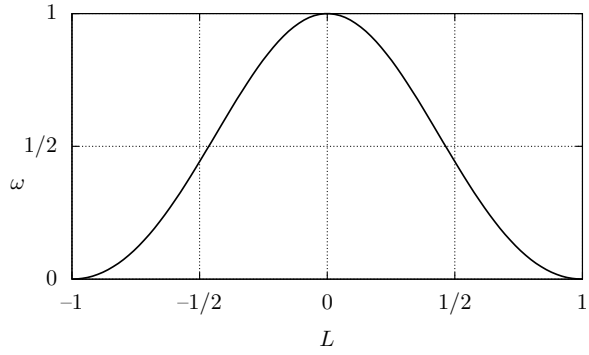

Fig. 2.4: The function $\omega = \omega(L)$ for a general stress state

This general Lode parameter dependency of ω is shown in figure 2.4. As the stress triaxiality is a measure of hydrostatic stress, i.e. relates to the distance between the origin and the deviatoric plane in Haigh–Westergaard space, it is generally cyclic in

the function ω which is proportional to J_3 and thus a measure of deviatoric stress. The Lode parameter, on the other hand, is like ω also proportional to J_3 such that L and ω are coupled. These relations contribute to induce the fact that σ^*, L and σ_e span the stress space — just as well as σ_{I}, σ_{II} and σ_{III} do.

To show how this picture commutes with the ω, σ^* relation in plane stress [21], depicted in figure 2.2 (curve b) above, we add the hydrostatic stress to each of the equalities in eq. (2.24), together with invoking the trigonometric relations

$$\cos(a \pm b) = \cos a \cos b \mp \sin a \sin b$$

with $a = \pi/6$ and $b = \vartheta$ and

$$\cos\vartheta = \frac{1}{1+\tan^2\vartheta}, \qquad \sin\vartheta = \frac{\tan\vartheta}{1+\tan^2\vartheta}$$

to obtain an expression for the principal stresses in terms of the Lode parameter:

$$\begin{aligned}
\sigma_{\mathrm{I}} = \sigma_e\left(\sigma^* + \frac{1}{3}\left(\sqrt{3}\cos\vartheta - \sin\vartheta\right)\right) &= \sigma_e\left(\sigma^* + \frac{3-L}{3\sqrt{3+L^2}}\right) \\
\sigma_{\mathrm{II}} = \sigma_e\left(\sigma^* + \frac{2}{3}\sin\vartheta\right) &= \sigma_e\left(\sigma^* + \frac{2L}{3\sqrt{3+L^2}}\right) \\
\sigma_{\mathrm{III}} = \frac{1}{3}\sigma_e\left(\sqrt{3}\cos\vartheta + \sin\vartheta\right) &= \sigma_e\left(\sigma^* - \frac{3+L}{3\sqrt{3+L^2}}\right)
\end{aligned} \tag{2.27}$$

By equating each of the rightmost expressions of eq. (2.27) to zero we obtain three different relations between σ^* and L that holds for three respective intervals of σ^*, given plane stress:

$$\sigma^* = \sigma^*(L) = \begin{cases} \dfrac{L-3}{3\sqrt{3+L^2}}, & -2/3 < \sigma^* < -1/3 \\ \dfrac{-2L}{3\sqrt{3+L^2}}, & -1/3 < \sigma^* < 1/3 \\ \dfrac{3+L}{3\sqrt{3+L^2}}, & 1/3 < \sigma^* < 2/3 \end{cases} \tag{2.28}$$

This relation is plotted in figure 2.5. Now using eq. (2.28) together with eq. (2.26) we plot the possible (ω, σ^*, L) states in plane stress, as well as the complete ω surface, in figure 2.6. This figure shows that the plane stress induced ω, σ^* relation, as plotted in figure 2.2 (curve b), is nothing but the projection of possible (ω, σ^*, L) states in plane stress onto a plane of constant L. Thus it is clear that ω is independent of σ^* in general, just not in the case of constraining the stress state to be plane.

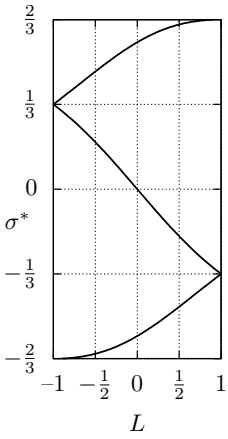

Fig. 2.5: The possible σ^*, L combinations in plane stress states.

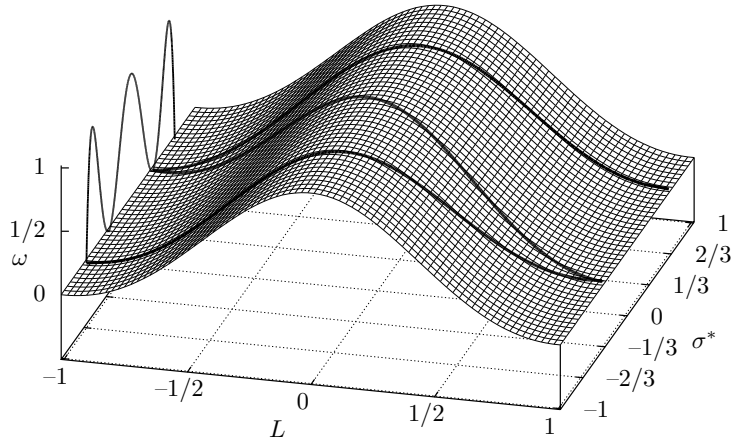

Fig. 2.6: The function $\omega = \omega(L)$ for a general stress state in σ^*, L space. The condition for plane stress (figure 2.5) is shown as the thick line on the ω surface, with a projection onto the $L = -1$ plane producing a graph identical to the plot in figure 2.2 (curve b).

2.6 A scalar approach for integration of the modified Gurson model constitutive relations

In this section it is described how one can integrate the modified Gurson model constitutive equations during prescribed straining of material (or an element in a FE model) using the scalar variables σ_m, σ_M and σ^* only. To do this one could make the assumption described in section 2.5.1 that there is a one-to-one relationship between the stress triaxiality value and the stress state being either plane or axisymmetric.

Assume that a piece of voided material is strained to a macroscopic equivalent plastic strain ε_e^P. A flow stress model, such as the power law, could be used to approximate the equivalent matrix stress σ_M of the material, calculated from its actual (microscopic/matrix) equivalent plastic strain ε_M^P,

$$\sigma_M = A + B\left(\varepsilon_M^P\right)^n$$

(given calibrated power law parameters A, B and n). This ε_M^P can be calculated by invoking power conjugacy between the macroscopic and microscopic entities, i.e.

$$\sigma_{ij}\dot{\varepsilon}_{ij}^P = \sigma_e\dot{\varepsilon}_e^P = (1-f)\sigma_M\dot{\varepsilon}_M^P$$

$$\boxed{\mathrm{d}\varepsilon_M^P = \frac{\sigma_e \mathrm{d}\varepsilon_e^P}{(1-f)\sigma_M}.} \tag{2.29}$$

A desired value of triaxiality $\sigma^* \equiv \sigma_m/\sigma_e$ of the material stress state could further be assumed, cf. the assumption of section 2.5.1, as mentioned above, that the value

of σ^* determines the stress state to be either plane or axisymmetric. Expressing σ_m and σ_e by the principal stresses σ_{I}, σ_{II} and σ_{III} gives

$$\sigma^* = \frac{\sigma_m}{\sigma_e} = \frac{\sqrt{2}}{3} \frac{(\sigma_{\mathrm{I}} + \sigma_{\mathrm{II}} + \sigma_{\mathrm{III}})}{\sqrt{[(\sigma_{\mathrm{I}} - \sigma_{\mathrm{II}})^2 + (\sigma_{\mathrm{I}} - \sigma_{\mathrm{III}})^2 + (\sigma_{\mathrm{II}} - \sigma_{\mathrm{III}})^2]}}. \tag{2.30}$$

Since the Gurson yield function depends on both σ_e and σ_m setting σ^* provides the necessary second equation for determining the stress state induced by the strain. Then, for a given equivalent plastic strain ε_e^P, the equivalent stress σ_e corresponding to ε_M^P can be calculated implicitly by (e.g. Newton-Raphson iterations) equating the Gurson yield function (2.12) to zero:

$$F(\sigma_e, \sigma_m, f) = \left(\frac{\sigma_e}{\sigma_M}\right)^2 + 2q_1 f \cosh\left(\frac{3q_2\sigma_m}{2\sigma_M}\right) - 1 - q_3 f^2$$

$$\boxed{F(\sigma_e, \sigma_m, f) = \left(\frac{\sigma_e}{\sigma_M}\right)^2 + 2q_1 f \cosh\left(\frac{3q_2\sigma_e\sigma^*}{2\sigma_M}\right) - 1 - q_3 f^2 = 0} \tag{2.31}$$

The yield surface gradient $\partial F/\partial\sigma_{ij}$

Let us begin with obtaining an expression for the yield surface gradient $\partial F/\partial\sigma_{ij}$ in terms of the desired scalar quantities σ_e, σ_M and σ^*. Inserting $\sigma_e\sigma^* = \sigma_m = \sigma_{kk}/3 = \sigma_{ij}\delta_{ij}/3$ in the second term, where δ_{ij} is the Kronecker delta, and using the chain rule in the first term, of eq. (2.31) we obtain

$$\begin{aligned}\frac{\partial F}{\partial\sigma_{ij}} &= \frac{\partial}{\partial\sigma_{ij}}\left[\left(\frac{\sigma_e}{\sigma_M}\right)^2 + 2q_1 f \cosh\left(\frac{q_2\sigma_{ij}\delta_{ij}}{2\sigma_M}\right) - 1 - q_3 f^2\right] \\ &= 2\frac{\sigma_e}{\sigma_M^2}\frac{\partial\sigma_e}{\partial\sigma_{ij}} + \delta_{ij}\frac{q_1 q_2 f}{\sigma_M}\sinh\left(\frac{q_2\sigma_{ij}\delta_{ij}}{2\sigma_M}\right)\end{aligned} \tag{2.32}$$

The equivalent strain derivative $\partial\sigma_e/\partial\sigma_{ij}$ is then calculated by using

$$\begin{aligned}\sigma_e &= \sqrt{3J_2} = \sqrt{\frac{3}{2}s_{ij}s_{ij}} \\ &= \sqrt{\frac{3}{2}(\sigma_{ij} - \frac{1}{3}\sigma_{kk}\delta_{ij})(\sigma_{ij} - \frac{1}{3}\sigma_{kk}\delta_{ij})}\end{aligned}$$

such that

$$\begin{aligned}\frac{\partial\sigma_e}{\partial\sigma_{ij}} &= \frac{\frac{3}{2}(\sigma_{ij} - \frac{1}{3}\sigma_{kk}\delta_{ij})\cdot 2}{2\sqrt{\frac{3}{2}(\sigma_{ij} - \frac{1}{3}\sigma_{kk}\delta_{ij})(\sigma_{ij} - \frac{1}{3}\sigma_{kk}\delta_{ij})}} \\ &= \frac{3}{2}\frac{s_{ij}}{\sigma_e}.\end{aligned} \tag{2.33}$$

Insertion of eq. (2.33) into eq. (2.32) finally yields

$$\frac{\partial F}{\partial \sigma_{ij}} = 3\frac{s_{ij}}{\sigma_M^2} + \delta_{ij}\frac{q_1 q_2 f}{\sigma_M}\sinh\left(\frac{q_2\sigma_{kk}}{2\sigma_M}\right). \tag{2.34}$$

Using the obtained expression (2.34) we also compute

$$\begin{aligned}\sigma_{ij}\frac{\partial F}{\partial \sigma_{ij}} &= 3\frac{s_{ij}s_{ij}}{\sigma_M^2} + \sigma_{mm}\frac{q_1 q_2 f}{\sigma_M}\sinh\left(\frac{q_2\sigma_{kk}}{2\sigma_M}\right) \\ &= 2\left(\frac{\sigma_e}{\sigma_M}\right)^2 + 3q_1 q_2 f\sigma^*\frac{\sigma_e}{\sigma_M}\sinh\left(\frac{3q_2\sigma^*}{2}\frac{\sigma_e}{\sigma_M}\right).\end{aligned} \tag{2.35}$$

The plastic multiplier $\dot{\lambda}$

The plastic multiplier $\dot{\lambda}$ needs also to be expressed by σ_e, σ_M and σ^* only. Using the associated flow rule (2.15) and multiplying with σ_{ij} on both sides yields

$$\sigma_{ij}\dot{\varepsilon}_{ij}^P = \dot{\lambda}\sigma_{ij}\frac{\partial F}{\partial \sigma_{ij}}.$$

Now, simply by invoking power conjugacy and inserting the expression for the inner product $\sigma_{ij}\partial F/\partial\sigma_{ij}$ from eq. (2.35), we obtain

$$\begin{aligned}\sigma_{ij}\dot{\varepsilon}_{ij}^P &= \sigma_e\dot{\varepsilon}_e^P \\ &= \dot{\lambda}\sigma_{ij}\frac{\partial F}{\partial \sigma_{ij}} \\ &= \dot{\lambda}\left[2\frac{\sigma_e^2}{\sigma_M^2} + 3fq_1q_2\sigma^*\frac{\sigma_e}{\sigma_M}\sinh\left(\frac{3q_2\sigma^*}{2}\frac{\sigma_e}{\sigma_M}\right)\right] \\ \boxed{\Leftrightarrow \mathrm{d}\lambda &= \frac{\sigma_e \mathrm{d}\varepsilon_e^P}{2\left(\frac{\sigma_e}{\sigma_M}\right)^2 + 3fq_1q_2\sigma^*\frac{\sigma_e}{\sigma_M}\sinh\left(\frac{3q_2\sigma^*}{2}\frac{\sigma_e}{\sigma_M}\right)}.}\end{aligned} \tag{2.36}$$

The increase in void volume fraction $\dot{f}$

As for all the constitutive relations it is desired that the stress state dependency of the void volume fraction increase given by eq. (2.13) is incorporated solely through the scalar variables σ_e, σ_M and σ^*. Let us therefore look at the inner product $s_{ij}\dot{\varepsilon}_{ij}^P$ appearing in the second term of the right hand side of eq. (2.13). An explicit expression for $s_{ij}\dot{\varepsilon}_{ij}^P$ can readily be obtained [19] by using the associated flow rule

(2.15), the expression for the yield function gradient (2.34) and $\sigma_e = \sqrt{\frac{3}{2} s_{ij} s_{ij}}$, viz.

$$\begin{aligned} s_{ij}\dot{\varepsilon}^P_{ij} &= s_{ij}\dot{\lambda}\frac{\partial F}{\partial \sigma_{ij}} \\ &= s_{ij}\dot{\lambda}\left[3\frac{s_{ij}}{\sigma_M^2} + \delta_{ij}\frac{q_1 q_2 f}{\sigma_M}\sinh\left(\frac{q_2\sigma_{kk}}{2\sigma_M}\right)\right] \\ &= 3\dot{\lambda}\frac{\overbrace{s_{ij}s_{ij}}^{=2\sigma_e^2/3}}{\sigma_M^2} + \overbrace{s_{ij}\delta_{ij}}^{=0}\dot{\lambda}\frac{q_1 q_2 f}{\sigma_M}\sinh\left(\frac{q_2\sigma_{kk}}{2\sigma_M}\right) \\ &= 2\dot{\lambda}\frac{\sigma_e^2}{\sigma_M^2}, \end{aligned} \tag{2.37}$$

where we have used that the trace of the stress deviator $s_{ij}\delta_{ij} = s_{kk} = 0$. Similarly, sslo looking at the volumetric plastic strain ε^P_{kk} by inserting eq. (2.34) into the associated flow rule (2.15) we have

$$\begin{aligned} \varepsilon^P_{kk} &= \dot{\lambda}\frac{\partial F}{\partial \sigma_{kk}} \\ &= \dot{\lambda}\left[3\frac{s_{kk}}{\sigma_M^2} + \delta_{kk}\frac{q_1 q_2 f}{\sigma_M}\sinh\left(\frac{q_2\sigma_{kk}}{2\sigma_M}\right)\right] \\ &= 3\frac{q_1 q_2 f}{\sigma_M}\sinh\left(\frac{q_2\sigma_{kk}}{2\sigma_M}\right). \end{aligned} \tag{2.38}$$

Inserting eqs. (2.37) and (2.38) in eq. (2.13) finally yields the void volume fraction growth

$$\begin{aligned} \dot{f} &= (1-f)\dot{\varepsilon}^P_{kk} + f k_\omega \omega(\sigma_{ij})\frac{s_{ij}\dot{\varepsilon}^P_{ij}}{\sigma_e} \\ &= \dot{\lambda}(1-f)\frac{3 f q_1 q_2}{\sigma_M}\sinh\left(\frac{3 q_2 \sigma_m}{2\sigma_M}\right) + \dot{\lambda} f k_\omega \omega(\sigma_{ij})\frac{2\sigma_e}{\sigma_M^2} \\ \boxed{\mathrm{d}f} &\boxed{= \mathrm{d}\lambda\left[(1-f)\frac{3 f q_1 q_2}{\sigma_M}\sinh\left(\frac{3}{2} q_2 \sigma^* \frac{\sigma_e}{\sigma_M}\right) + f k_\omega \omega(\sigma_{ij})\frac{2\sigma_e}{\sigma_M^2}\right].} \end{aligned} \tag{2.39}$$

2.6.1 Investigation of model characteristics

Utilizing the boxed eqs. (2.21) (or (2.26)), (2.29), (2.31), (2.36) and (2.39) which all are expressions depending on the stress state through σ_e, σ^* and σ_M only (except eq. (2.26)) , one can build a numerical procedure to e.g. calculate the development of void growth and equivalent stress in a piece of material, e.g when strained at a constant value of triaxiality σ^* under plane stress.

A pseudo code for such a procedure could be as follows.

– Set material parameters, e.g. A, B, n, f_0, q_1, q_2 and k_ω
– Declare an array of values for ε_e^P, e.g. $\{0.00, 0.01, 0.02, ..., 1.99, 2.00\}$
– Set the value for σ^*, e.g. $\sigma^* = 0.5$
– Calculate $\omega(\sigma^*)$ by eq. (2.21) (assuming plane stress)
– Set/declare $\varepsilon_M^P = f = \sigma_M = \sigma_e = \Delta\lambda = 0$
– **For** the chosen values of ε_e^P
    – Calculate $\sigma_M = A + B\left(\varepsilon_M^P\right)^n$
    – Set $\sigma_e = \sigma_M$ as an approximation
    – Using e.g. Newton–Raphson iterations, calculate σ_e to the desired accuracy by equating the yield function (2.31) to zero
    – Calculate $\Delta\lambda$ by eq. (2.36)
    – Calculate $\Delta\varepsilon_M^P$, and then update ε_M^P, by eq. (2.29)
    – Calculate Δf, and the update f, by eq. (2.39)

End

A MATLAB implementation, given in appendix A, of the pseudo code yielded the data presented in figure 2.7. Now — using an instability or fracture criterion, namely $\mathrm{d}\sigma_e/\mathrm{d}\varepsilon_e^P = 0$ — one could use a such numerical procedure for a number of different stress triaxialities to obtain a strain-triaxiality fracture locus. The result of that approach is presented in figure 2.8.

Table 2.1: Material parameters used in figures 2.7 and 2.8

A	B	n	f_0	q_1	q_2
$1.25 \cdot 10^9$	$2 \cdot 10^8$	0.3	$2 \cdot 10^{-3}$	1.5	1

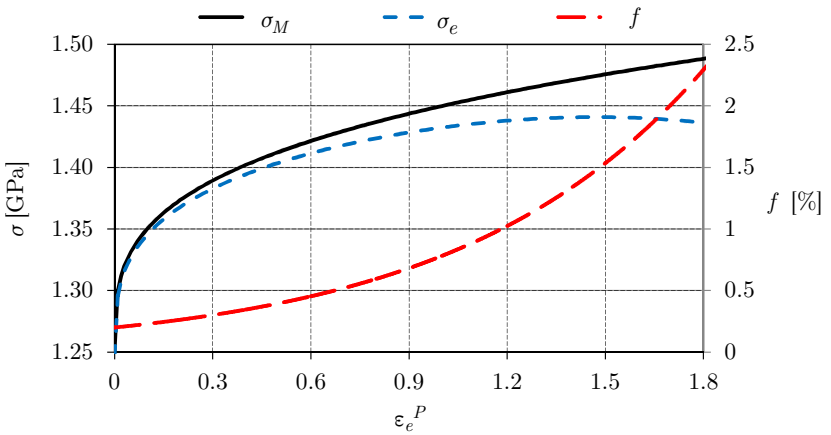

Fig. 2.7: Example of the evolution of the microscopic and macroscopic equivalent stress and the void volume fraction in the extended Gurson model. Here $k_\omega = 2$ while the other parameter values were set according table 2.1. Additionally the triaxiality was set to $\sigma^* = 0.1$

.

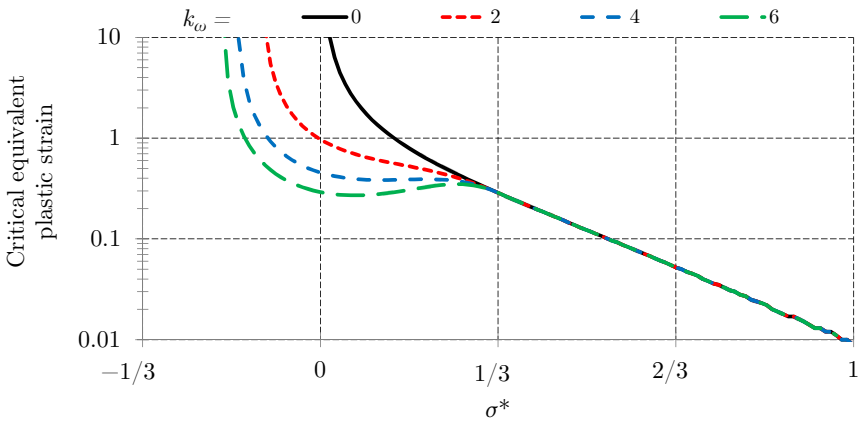

Fig. 2.8: Estimated triaxiality fracture locus for the extended Gurson model assuming plane stress states for $|\sigma^*| < 1/3$ and axisymmetric stress states for $\sigma^* > 1/3$, where the critical strain was set to the value of strain giving $\mathrm{d}\sigma_e/\mathrm{d}\varepsilon_e^P = 0$, corresponding to $\varepsilon_e^P \approx 1.5$ in figure 2.7. Parameter values were set according to table 2.1.

Chapter 3
Material tests

In order to get the data necessary to adjust the parameters of the Gurson model tensile tests, shear tests and plane strain tests were carried out at SIMLab. Three different materials were considered; Weldox® 460E (W460E), Weldox® 700E (W700E) and Weldox® 900E (W900E). The effects of strain rate and temperature have been studied earlier [12], and these parameter values are assumed to fit directly into the Gurson model.

The process of calibrating the material model will be discussed in detail in chapter 4. This chapter describes the Weldox® steel alloys and the specimens, setups and results of the tests.

3.1 Weldox® steel alloys

Weldox® is an extra-high strength steel that combines its high strength with high ductility and good weldability, which enables production of strong but lightweight load bearing structures. This combination is obtained through a steel composition with low content of inclusions and through controlled rolling and heat treatment processes [12]. It is delivered with different strengths, with guaranteed nominal yield stresses ranging from 500 to 1300 MPa [31]. One of the three alloys considered in this thesis, W460E, is no longer produced as it is replaced with a new product, Weldox® 500E. But it is nonetheless considered because of the strong connection with the studies of Dey [12].

W460E belongs to the TM steels, which means that the steel obtains its strength and toughness by an advanced thermomechanical rolling and/or controlled cooling procedure. W700E and W900E are in a group termed as QT, that goes through a significant quenching and temperature process [12]. Table 3.1 gives the chemical composition of the three alloys.

3.2 Tensile tests

All tests, both the tests done earlier by Dey [12] and the tests done in connection with the work with this thesis, were done quasi-statically and performed at room temperature. In order to achieve quasi-static deformation the displacement rate

Table 3.1: Nominal chemical compositions (in weight %) of W460E [12], W700E and W900E[31]

	460E	700E	900E
C	0.16	0.20	0.20
Si	0.50	0.60	0.50
Mn	1.70	1.60	1.60
P	0.025	0.020	0.020
S	0.015	0.010	0.010
B	–	0.005	0.005
Nb	0.050	0.040	0.040
Cr	–	0.70	0.70
V	0.10	0.090	0.060
Cu	–	0.30	0.10
Ti	0.020	0.040	0.040
Al	0.015	0.015	0.018
Mo	0.050	0.70	0.70
Ni	0.10	2.0	0.10
N	0.015	0.010	0.010

were set to give an initial strain rate at approximately $5 \cdot 10^{-4}$ s^{-1} in the shear stress and plane strain tests. In the axisymmetric tests performed by Dey [12] the displacement rates were set such that an average strain rate in the order of 10^{-3} s^{-1} was achieved. The plane strain and shear stress tests were done three time for each steel alloy, while for the axisymmetric tests only one representatively selected data series from each test type and alloy was available to the authors, consisting of values of applied load, cross-head displacement and diameter reduction measured with a one second interval.

3.2.1 Axisymmetric tests

Axisymmetric tensile tests were performed on cylindrical specimens. Tests of smooth specimens would provide data necessary to determine the plastic hardening parameters in the material model, and complementing with notched specimens giving different states of triaxiality a good basis for determining also the void volume fraction parameters is achieved. This is because the void volume fraction parameters to a high degree affect the fracture displacement of these tests. Notched tensile tests with the three different notch radii 2.0, 0.8 and 0.4 mm were performed for all three steel alloys. The geometry of the smooth and notched specimens are shown in figure 3.2, where R depicts the mentioned notch radii and the angle α is zero for the specimens with notch radius 2.0 and 17.5˚for the specimens with notch radius 0.8 and 0.4 mm. The experimental results from smooth and notched specimen tests are shown in figure 3.1.

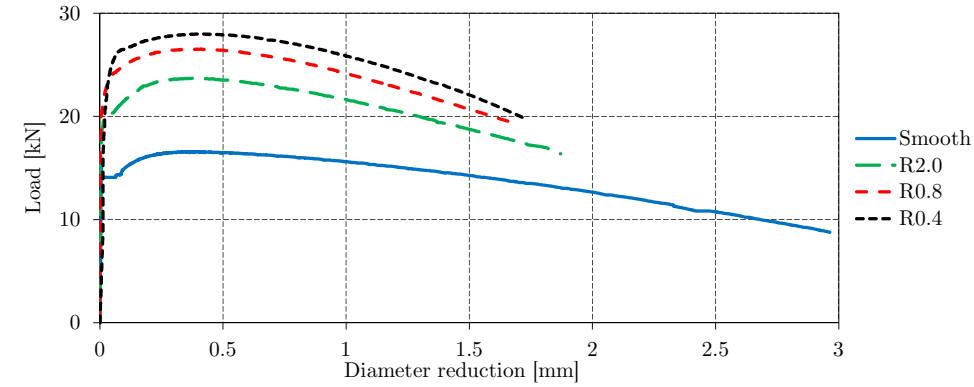

(a) W460E

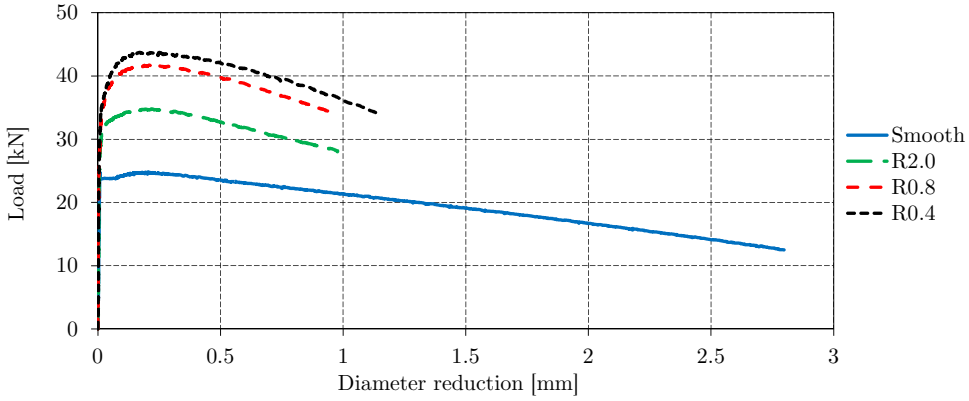

(b) W700E

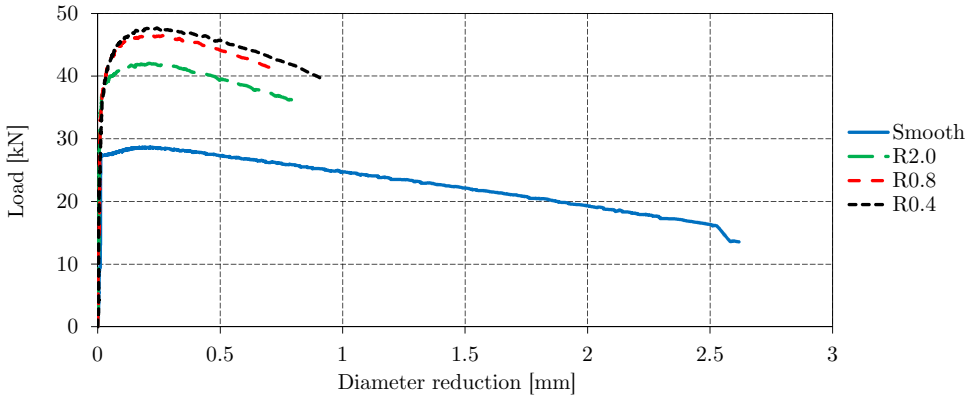

(c) W900E

Fig. 3.1: Data from tensile tests with smooth and notched specimens. The notch radius r is indicated as Rr in the legends.

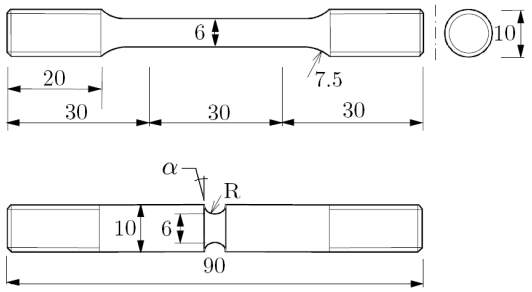

Fig. 3.2: Smooth and notched test specimen geometries with dimensions in millimeter. The radius R is the notch radius varying between 0.4, 0.8 and 2.0 mm, and the angle α was equal to zero in the $R = 2.0$ specimen while $\alpha = 17.5°$ for the $R = 0.8$ and $R = 0.4$ mm specimens.

3.2.2 Shear tests

In a state of plane stress, $\omega(\sigma^*) \approx 1$ for $\sigma^* \approx 0$, according to eq. (2.21), and hence the value of k_ω is significant for the material behavior. Such a stress state is achieved by performing a shear stress test using a specimen with geometry as shown in figure 3.3, and thus the value of k_ω can be obtained from inverse modeling of the test.

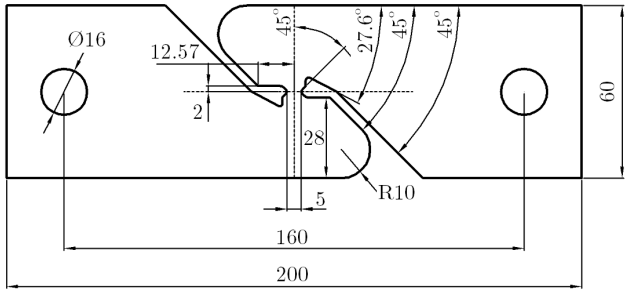

Fig. 3.3: Geometry of the shear stress test specimens. Dimensions are in millimeters.

The specimen was mounted in the machine by putting bolts through the holes in the side plates. Applied load, cross-head displacement and extensometer displacement were measured with a frequency of ~ 10 Hz during each test. In addition the strain field in the mid area of the specimen were recovered after-hand using digital image correlation (DIC)[1] on images of the specimen taken with a frequency of 1 Hz.

[1] For more information on DIC, see [16].

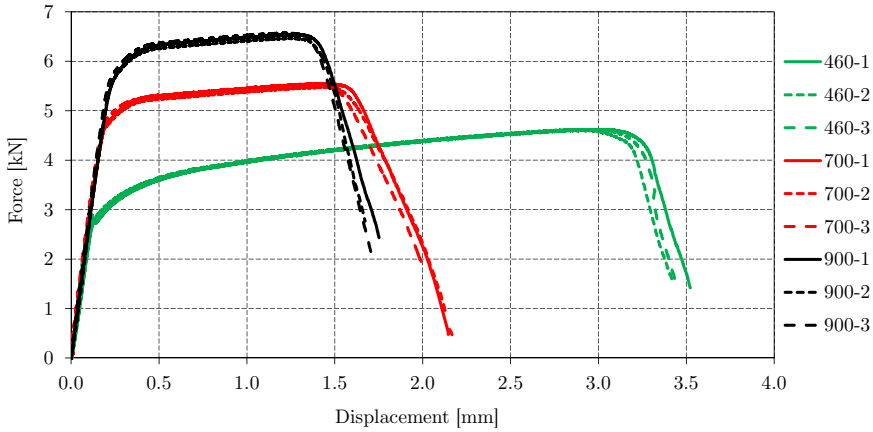

Fig. 3.4: Shear stress test results. Steel alloy type and test number is marked as 'alloy'-'test no.'.

3.2.3 Plane strain tests

In order to adjust the value of k_ω it was done *plane strain* tests in addition to the shear stress tests described above. The state of plane strain is achieved due to the width of the specimen (with geometry shown in figure 3.5) being very large compared to the thickness in the parallel section. Because of this the resistance against transversal contraction in the direction marked with a 'T' in figure 3.5 is large enough to avoid strains in that direction, and hence the parallel area of the specimen experiences a state of plane strain. But since the strain is of low magnitude in the width direction, the stress in that direction must be close to half of the longitudinal stress, while the stress in the thickness direction is low since in that direction the parallel area can contract freely. This means that the stress state is on the form $\sigma_{\mathrm{II}} \approx \sigma_{\mathrm{I}}, \sigma_{\mathrm{III}} \approx 0$ and it is evident from the definition of the Lode parameter L in eq. 2.22 that $L \approx 0$ and therefore $\omega(\sigma_{ij}) \approx 1$ form eq. 2.26. It is on this basis, in terms of the modified Gurson model, that plane strain tests to a great extent are influenced by the value of k_ω.

The specimens used in the plane strain tests conducted had a geometry as shown in figure 3.5. In the test set up, the two thicker parts of the specimen were clamped to the test machine, as shown in figure 3.6.

During each test applied load, cross-head displacement and extensometer displacement were measured. Additionally, with a frequency of ~ 1 Hz, pictures were taken of the specimens' parallel area in order to perform DIC analysis after-hand. The force–displacement data recorded is shown in in figure 3.7.

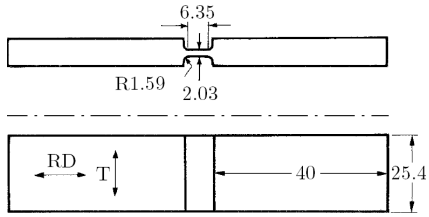

Fig. 3.5: Plane strain test geometry. RD and T marks rolling direction and plate thickness direction respectively.The parallel section is ground parallel to the T direction.

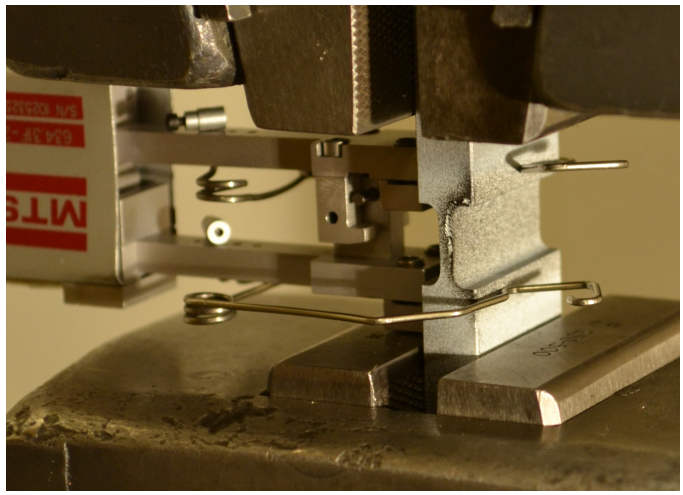

Fig. 3.6: Plane strain test specimen clamped to test machine.

3.3 Discussion

The plane strain test set up had an important source of error. When clamping the side plates of the specimen to the test machine, there might be a small angle between the longitudinal direction of the specimen and the loading direction of test. As a consequence, the test results will vary for different angles, and it was evident that this angle could alter the fracture mechanism of the specimen. When the specimen was mounted with a such angle being to big the fracture became *a*symmetric and more brittle than if it was symmetric. The symmetric and *a*symmetric fracture patterns are shown in figure 3.8. Figure 3.7 shows that the two only specimens that had a symmetric fracture — 460–2 and 460–3 — endured a significantly larger displacement than the other W460E specimen, and suggests that a similar fracture tail in the force–displacement data for W700E and W900E could have been recovered if some of these specimens were mounted with a small enough angle to the load direction. In afterthought, this fact seems to suggest that the lower degree of ductility

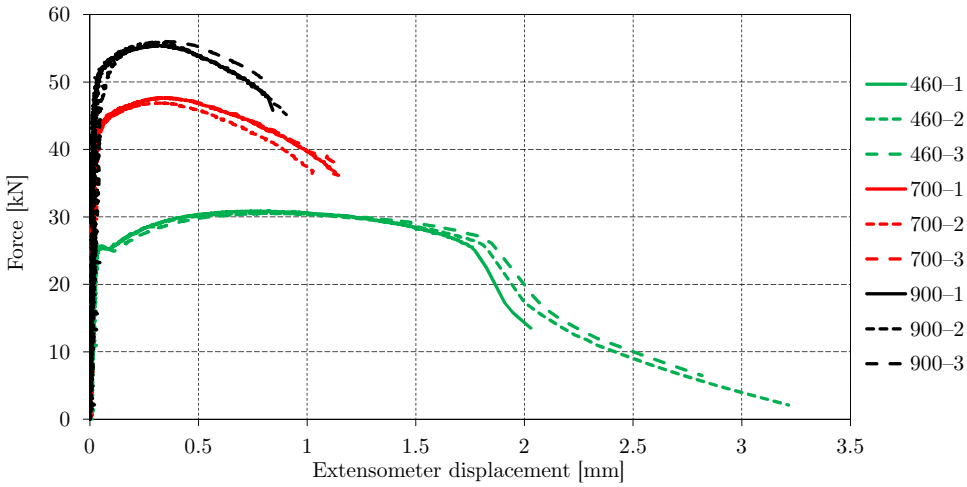

Fig. 3.7: Plane strain test results. Steel alloy type and test number is marked as 'alloy no.'-'test no.'.

in W700E and W900E causes a higher sensitivity for slant mounting. One solution to this problem could be to alter the specimen geometry by decreasing the length of the parallel section, while another solution could be to redesign and dimension the specimen so that clamping of the ends is not the only possible mounting alternative.

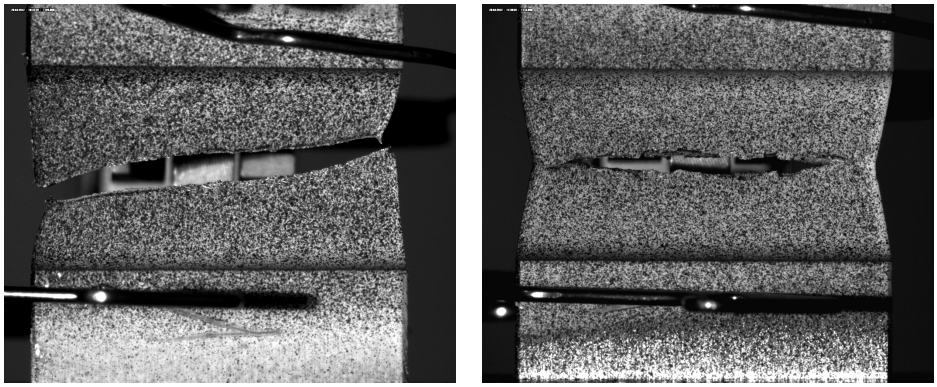

(a) 460–1 (after fracture) (b) 460–2 (during fracture)

Fig. 3.8: Plane strain test specimens with straight and slanted fracture

For the shear stress tests, on the other hand, such mounting problems were not present since the cross section of the yielding area of the specimen is small. As seen in the results in section 3.2.2, the results for the shear tests correspond well with each

other. On the other hand the test specimen geometry causes true-strain–true-stress data to be impossible to calculate from a set of force-displacement data. In order to obtain such data from the shear stress test DIC must be used. For the purpose of this thesis, however, force-displacement data sufficed. All in all the experimental results for all tests shows decent correspondence with each other. Together they constitute the basis for calibration of the parameters in the material model that will be used for numerical simulations of ballistic impact.

Chapter 4
Material model calibration

In order to describe the material behavior of each of the three steel alloys to be studied with the extended Gurson model, a number of parameter values had to be determined — namely the Voce hardening parameters (σ_0, Q_1, θ_1, Q_2, θ_2), initial and critical void volume fraction (f_0, f_{cr}) and the parameter for scaling the shear stress influence on the material damage (k_ω). All these parameters were adjusted by performing FEM simulations of the tensile tests described in chapter 3 and comparing the results. In all simulations (also impact simulations described in chapter 6) the element size was chosen to be consistent with other simulations, choosing an element area (smallest face are for solid elements) to be ≈ 0.01 mm^2. This chapter describes this calibration process in detail. Parameters controlling influence of strain rate hardening (C), temperature softening (m) and adiabatic heating (β_{TQ}), on the other hand, were taken, by advice from the supervisors, as found though earlier studies and experiences.

4.1 Comments on the implementation of the modified Gurson model

For the work with this thesis an LS–DYNA *'user material sub-routine'* (UMAT) made by Torodd Berstad[1] was used in order to use the modified Gurson model with the LS–DYNA finite element code.

Generally such UMAT's work as stand-in algorithms for LS–DYNA to calculate the update in the stress components *given* an update in strain components. Other than this the LS–DYNA finite element code remains unchanged under an interchange of one UMAT to another, and does itself contain the algorithms for iterating over elements, setting up strain component updates, contact, etc. However, in addition to updating stress components the UMAT specifies which history data/variables that should be saved, and it can also override the strain increments specified by the main code.

The UMAT used in the work with this thesis uses explicit time integration on model level, but has a semi-implicit algorithm for stress calculation in each integration point. By semi-implicit it is here meant that the plastic multiplier is found by

[1]Research scientist Torodd Berstad at SIMLab, Department of Structural Engineering, NTNU. E-mail: torodd.berstad@ntnu.no

implicit iterations (or with a backward Euler scheme) by using an *updated* yield surface gradient, while the plastic flow direction in stress space is found explicitly (or by forward Euler iterations) by using an *initial* yield surface gradient. Thus the algorithm does not involve solving equilibrium equations and is hence not formally implicit.

Further on, two subtle yet very important improvements were made during the work with this thesis in order to make the UMAT numerically stable and versatile.

1) An explicit demand for the void volume fraction being positive was applied. More specifically, when the void volume fraction is calculated by eq. (2.13) as, say, $f_{n+1}^{(2.13)}$, then the UMAT potentially overrides this calculation as it always sets the new value of the void volume fraction according to

$$f_{n+1} = \max\{0, f_{n+1}^{(2.13)}\}.$$

This is necessary in extreme cases of compression (such as the initial part of a penetration process) where the void volume fraction decreases (according to eq. (2.13)). Then it is possible, due to discretization, that the void volume fraction change is a slightly larger negative amount than the value of the void volume fraction itself, so that it is evaluated to number slightly below zero. When this happens the void volume fraction eventually diverges to $-\infty$ and the solution is no longer valid.

2) Sub-stepping over the strain increment given by LS–DYNA was set to be performed when the norm of the incremental strain tensor, say, $||\Delta\varepsilon_{ij}||$, is larger than $5 \cdot 10^{-5}$. Specifically the UMAT divides the six strain component increments equally into n parts when the norm of the incremental strain tensor is n times larger (rounded to nearest integer) than $5 \cdot 10^{-5}$. This is done in a outer for loop which iterates from 1 to n. In each sub-step the time is incremented correspondingly to account for strain rate dependency.

Another important aspect of implementing the Gurson model is that if the void volume fraction is allowed to take on large values (e.g. $\sim 20\%$), problems can be encountered when the ratio of von Mises stress to the hydrostatic stress becomes very small. This leads to a almost purely hydrostatic increment of the flow stress, resulting from the associated flow rule and the yield surface taking the most extreme form shown in figure 4.1, which literally means that the element is exploding.

It was considered eroding elements reaching such stress states (i.e. witnessing total loss of shear strength before the critical void volume fraction f_{cr} is reached) to avoid divergence of the plasticity algorithm, and this was the case at the time when the material model calibration work in this thesis was conducted. However, this element erosion criterion was removed later on and was not present during penetration simulations described in chapter 6. This means that the combination

of high void volume fraction and values of the ratio shear stress to hydrostatic stress very close to zero had to be avoided.

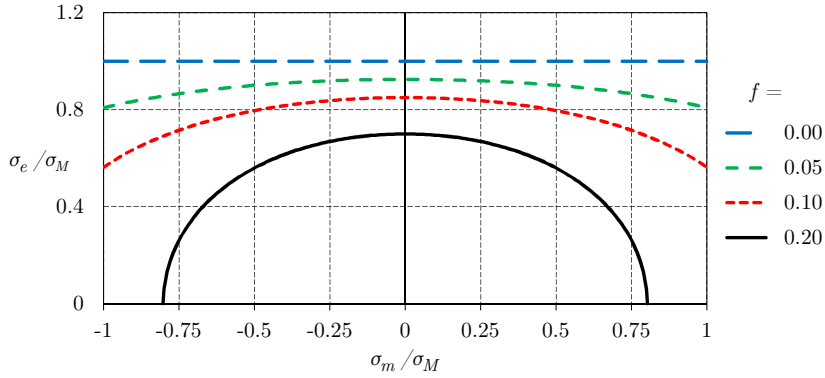

Fig. 4.1: Plot of the Gurson model yield surface given by eq. (2.12) in normalized σ_e, σ_m space, i.e. σ_e/σ_M as a function of σ_m/σ_M at yielding with $F = 0$.

The construction of the UMAT can be summarized by the following pseudo code:

– Declaration of variables
– Fetch of data from element-model keyword file and validation of this fetching
– Fetch updated history variables
– Evaluate the norm of the incremental strain tensor $||\Delta\varepsilon_{ij}||$
– Set $n = \max\{1, ||\Delta\varepsilon_{ij}||/(5 \cdot 10^{-5})\}$
– **For** $i = 1$ to n
    – Increment each of the strain components with a factor of i/n of the respective strain component increment prescribed by LS–DYNA
    – Increment the time by a factor of i/n of the time step prescribed by LS–DYNA
    – Set up elastic trial state
    – Detect yielding elements (yield function greater than zero)
    – **For** all elastically stressed elements
        – Update stress components
    End
    – **For** all plastically stressed elements
        – Estimate effective plastic strain increment from viscoplasticity (yield surface expansion)
        – Iterate to compute the stress state (or stress components) and invariants, the function $\omega(\sigma_{ij})$, the plastic multiplier and the change in void volume fraction
        – Update stress components
    End
End
– Save new history variable values

4.2 Overview of the process

The values for strain rate hardening (C) and temperature softening (m) was determined based on the study of Dey showing that for the values for the steel alloys considered in this thesis ranged from 0.0079 to 0.0115 and from 0.893 to 1.131 for C and m, respectively [12]. For simplicity the values $C = 0.01$ and $m = 1$ was set for all three steel alloys. This was in order to enhance the comparability of the impact simulation results described in chapter 6.

All material tests were performed quasi-statically, which means that any heating of the specimens was assumed to be negligible. Hence all the material tests were simulated with Taylor-Quinney coefficient for adiabatic heating β_{TQ} set to zero.

Strain hardening and void volume fraction parameters
The Voce parameters and void volume fraction parameters were first approximated by analyzing the axisymmetric test results while the final adjustments was made using inverse modeling. Specifically, the data series of measured load and specimen diameter reduction were used to calculate a data series of true stress and true strain values. To take necking into account, true stress data were adjusted using Bridgman analysis. The final strain–stress data was then used to fit a Voce curve. Along with initially assumed values for f_0 and f_{cr}, these values were used in a simulation model of the smooth tests in LS-DYNA. Simulation results were then compared with experimental results, and certain parameters were adjusted accordingly until the results coincided with satisfying accuracy. In the following this is referred to as inverse modeling. An alternative approach is to use an optimization tool, such as LS-OPT [2], to fit parameter values automatically using e.g. least squares optimization. For the work with this thesis the manual approach was found to be sufficient.

Due to problems with simulations of ballistic impact on targets plates of the W460E alloy, the procedure for this specific material had to be altered. The problems were related to a high void volume fraction level, resulting from f_0 being set to high. This problem is discussed in section 4.6, but implied in summary that additional time had to be spent on calibrating the value f_0 and f_{cr} for W460E, along with adjustment of the Voce parameters. In retrospect, this should probably have been done for all three materials, but due to a strong time constraint the authors were not able to do this.

The parameter k_ω
Determination the value of k_ω, which scales the influence of the ω-function, i.e. the influence of shear stresses on the material damage evolution, was done by using the Voce parameters and the void volume fraction parameters in simulation models of

[2]LS-OPT is an extension tool used to, among other things, calibrate parameters using the LS-DYNA code. http://www.lsoptsupport.com/

the shear stress and plane strain test described in chapter 3. Independent k_ω values were obtained for each steel alloy using inverse modeling.

4.3 Use of axisymmetric test simulations

For each alloy, the calibration process started by using eqs. (2.3) and (2.5) together with the test results for the smooth specimen to calculate true-strain–true-stress data. For W460E, these data are shown as the solid line in figure 4.2.

As it can be seen in figure 4.2, the curve has a yield plateau due to a natural occurrence of pinning of dislocations in the material, that ends at $\varepsilon_l \approx 3\%$. This phenomenon is common for steel alloys and is there is seldom made efforts to recreate it in FEM simulations. The next step in adjusting the hardening parameters is here to do a Voce model curve fit of the stress–strain data. For simplicity, only the data points after the yield plateau were used. This will cause a slightly low yield stress σ_0 of the modeled hardering, but this error is negligible as it only affects a small part of the straining process.

In order to approximate true stress from force-displacement data after the necking strain, Bridgman analysis was applied to the true stress data. Thus the necking strain ε_n has to be determined, and this was done by determining numerically at which value of true strain eq. (2.7) was satisfied. Figure 4.2 shows that the value of ε_n for W460E was ≈ 14 %.

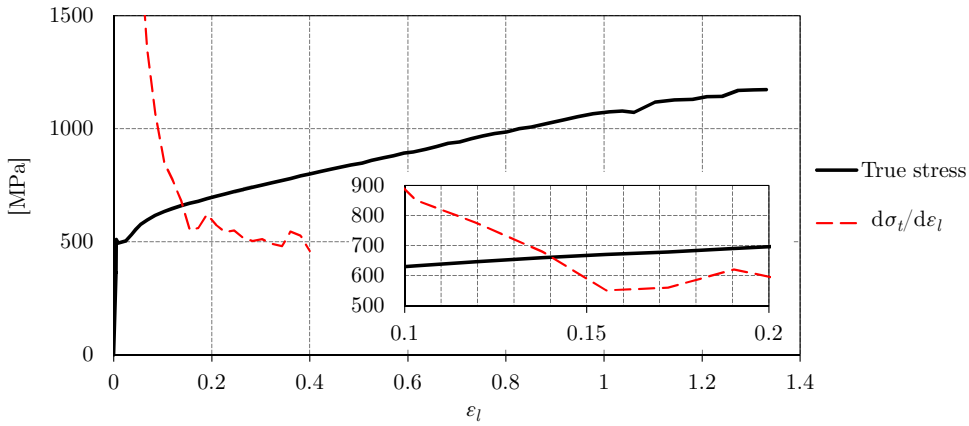

Fig. 4.2: True stress and differentiated true stress from the W460E smooth specimen test showing that the necking strain of the specimen was approximately 14%.

The true stress values for strains larger than ε_n was replaced with the new set of stress values calculated using the Bridgman formula (i.e. eq. 2.9). Comparison of

the true stress and the adjusted true stress is shown in figure 4.3.

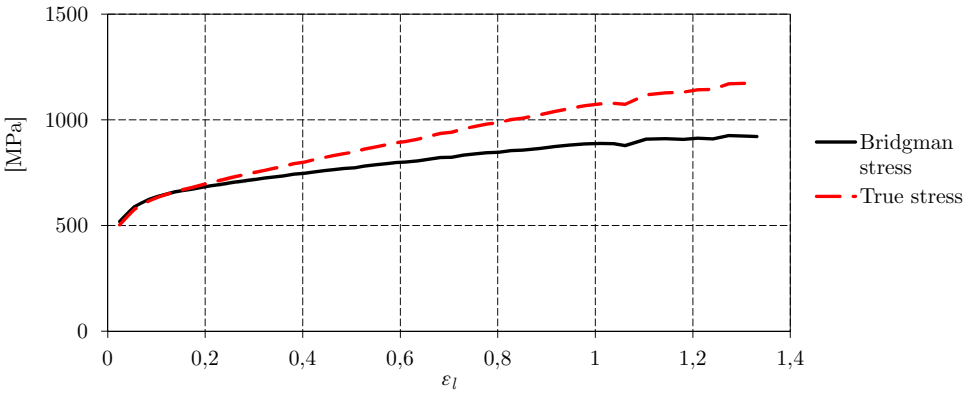

Fig. 4.3: Bridgman adjusted stress compared with true stress

As a result of the implementation of the modified Gurson model, the Voce law, described in section 2.2, has to be used to model the material work hardening. In order to do this one performs a curve fit of the analytical expression to the obtained stress-strain data, and this curve fit adjusts the hardening parameters directly. In this case the Microsoft Excel Solver function was used to do the curve fit. The resulting analytical stress-strain curve is compared to the Bridgman adjusted experimental data in figure 4.4.

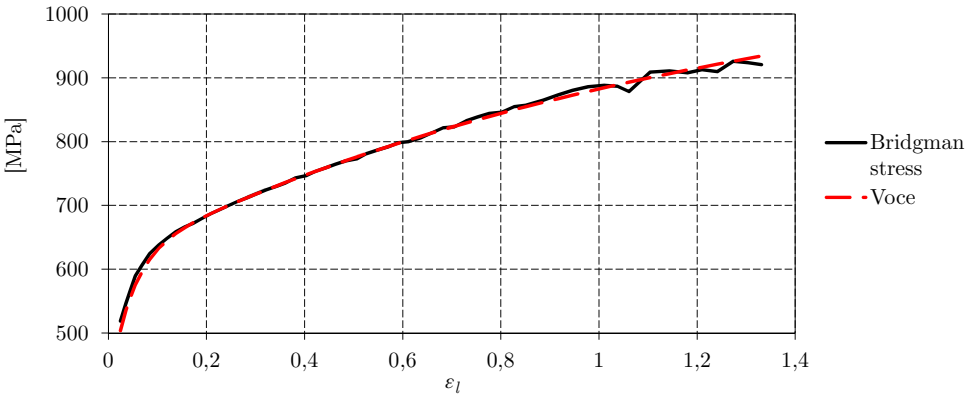

Fig. 4.4: Voce curve fitted to Bridgman adjusted true stress

The set of Voce parameters, obtained through curve fitting of the Bridgman corrected true-stress–true-strain data, are given in table 4.1.

The next step was to determine the void volume parameters, namely f_0 and f_{cr}. The results of Koplik and Needleman [22] suggests specifically that f_0 values of both 0.13 % and 1.04 % are possible, and thus f_0 were initially set to 0.5 % for all

Table 4.1: Initial Voce parameter values for W460E

$\sigma_0 =$	413.84 MPa
$Q_1 =$	201.45 MPa
$\theta_1 =$	4678.1 MPa
$Q_2 =$	491.53 MPa
$\theta_2 =$	387.44 MPa

three materials. The value for critical void volume was initially guessed to be about 15 %.

With an initial set of parameters for strain hardening and void volume fraction, a model for numerical simulation of the axisymmetric tensile tests was established. The meshes used is shown in figure 4.5. After necking the straining was expected to localize in the middle area of the specimen. Due to this the mesh was refined in this area, while the mesh was made a lot coarser in the rest of the specimen, to get accurate results while saving computational effort. The smallest elements, closest to the middle, were made rectangular in order for them to be as quadratic as possible near failure. The mesh configuration after fracture is shown in figure 4.6. Axisymmetric shell elements were used, and in addition to axisymmetric symmetry, symmetry about the longitudinal midpoint of the specimen was exploited by constraining the mid cross-section of the specimen to have zero displacement in the longitudinal direction. The displacement was applied in the top section of the specimen. In all simulations of axisymmetric tests, a mass scaling factor of 10^{10} was multiplied to the material density. Since explicit time integration was used, this will enlarge the critical time step and save computational time.

The first test of the material parameters was done by simulating a model of the smooth specimen in LS-DYNA. From the simulation, data for force in the top section (where displacement was applied) and the displacement in the radial direction of the node situated in the lower right corner of the mesh (which is equivalent to the part of the specimen where the diameter reduction was measured in the material tests). The force and diameter reduction data of the simulation were then combined and compared with the equivalent data from the experiments. For the W460E simulation with the initial parameter values, this comparison is shown in figure 4.7.

The comparison shows that the initial set of parameter values makes the material to soft in the plastic domain, especially after necking occurs. It is therefore necessary to adjust some of the values in order to correct this difference. Inserting the values given in table 4.1 into the Voce formulation it reads

$$R = 201.45\left(1 - \exp\left(-\frac{4678.1}{201.45}\varepsilon_l^P\right)\right) + 491.53\left(1 - \exp\left(-\frac{387.44}{491.53}\varepsilon_l^P\right)\right).$$

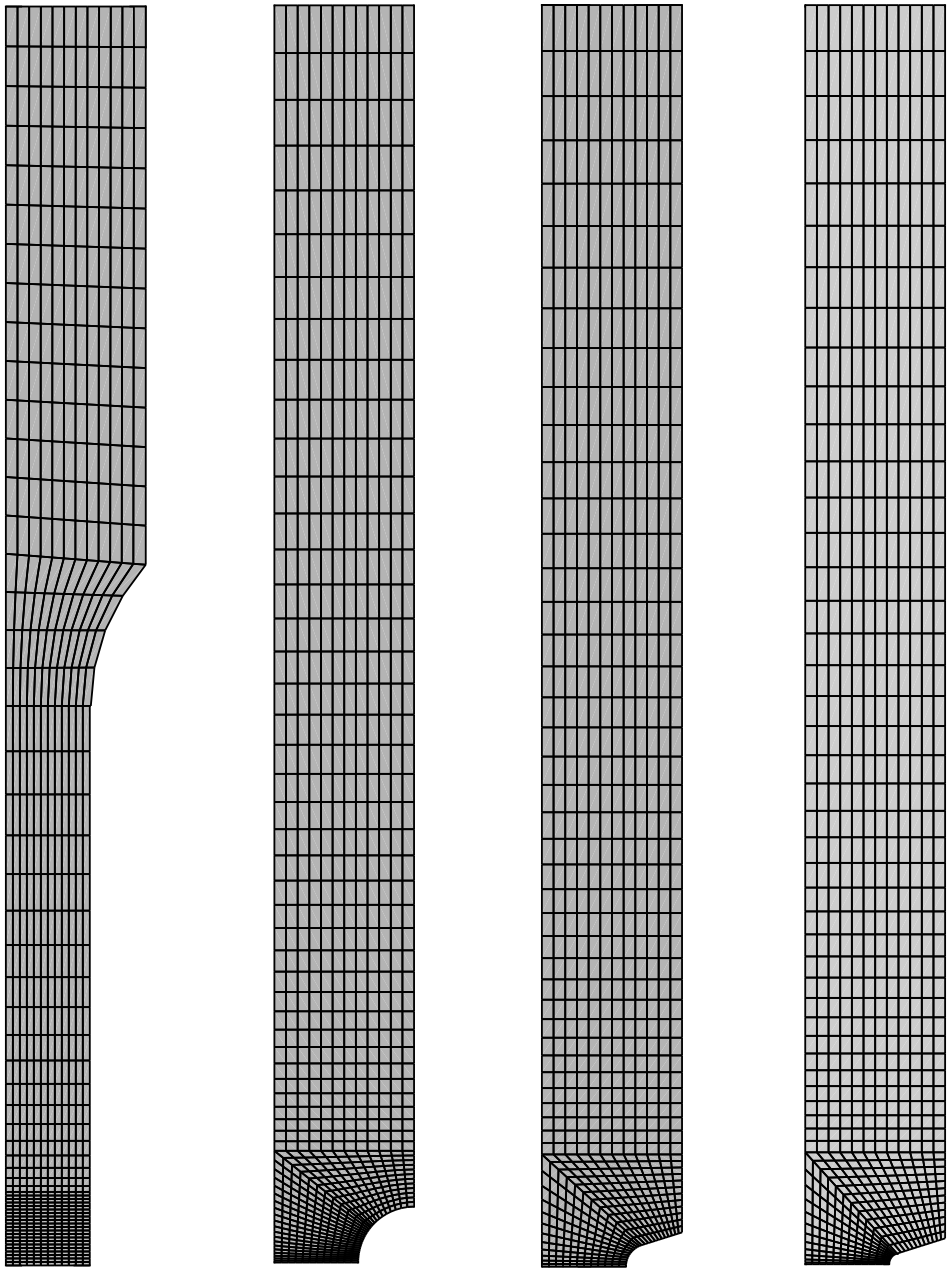

(a) smooth, 588 elements

(b) R2.0 mm notch, 864 elements

(c) R0.8 mm notch, 768 elements

(d) R0.4 mm notch, 768 elements

Fig. 4.5: Meshes used in tensile test simulations.

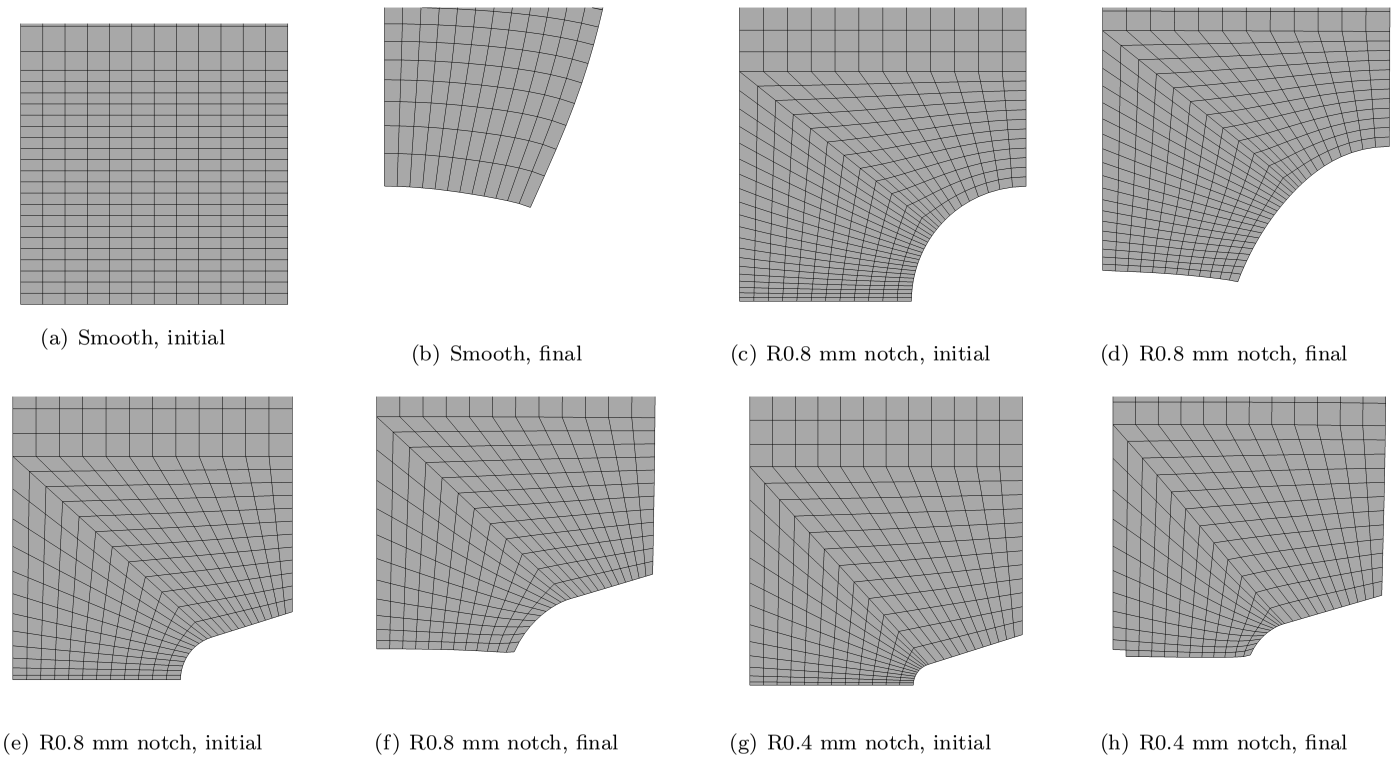

(a) Smooth, initial

(b) Smooth, final

(c) R0.8 mm notch, initial

(d) R0.8 mm notch, final

(e) R0.8 mm notch, initial

(f) R0.8 mm notch, final

(g) R0.4 mm notch, initial

(h) R0.4 mm notch, final

Fig. 4.6: Localization area mesh details from the axisymmetric tensile test simulations. The meshes are shown in their initial and final states, i.e. at zero displacement and just after fracture. The respective meshes are aligned such that one can see the magnitude of deformation. Please note the shape of the most distorted elements after fracture, as opposed to their initial shapes.

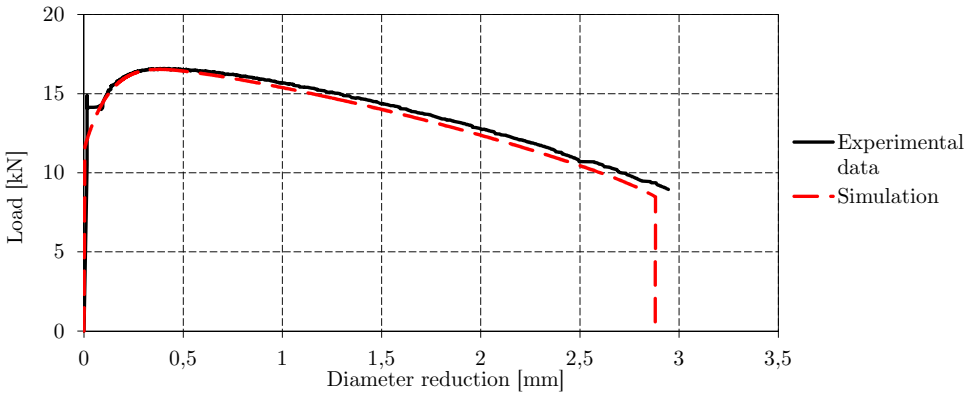

Fig. 4.7: Initial simulation results compared with experimental data

Each term in the formula approaches the value of their respective Q_i as the exponential function decreases for increasing ε_l^P. For big values of θ_i compared to Q_i, this happens quickly, as is the case for the first term, while the second term has a much smaller value for θ_i, which means it starts to contribute significantly to the value of R when the first paragraph has reached its maximum value. Because of this the curve is almost linearly asymptotic which also can be said of the stress–strain data. Taking one more look at figure 4.7 it is found that, when disregarding the yield plateau, the results coincide until necking. Because of this it was assumed that the first pair of values were satisfyingly accurate, while the second had to be adjusted. To get a less steep curve, the value of θ_2 had to be increased, in order to obtain the value of Q_2 earlier. The correct value of θ_2 was found by trial and error, where the value was adjusted and the model simulated, until the simulation result was satisfyingly accurate. This relation between the two paragraphs in the Voce formula (one big and one small θ_i) was found for all three alloys.

The value of f_0 set to 0.5 % gave satisfying results for both W700E and W900E, while it made the correct fracture displacement for the notched specimens impossible to obtain for W460E. In addition, f_0 set to 0.5 % were problematic in the impact simulations, as mentioned in section 4.2. When inspecting the tesnion test simulation results in LS-PrePost it was found that the fracture happened before the critical elements reached a void volume fraction of f_{cr}. Instead the fracture came as a result of the (temporarily included) erosion criterion based on complete loss of shear strength, as discussed in section 4.1. Because of this, the fracture was independent of the critical void volume fraction, and thus adjustment of f_0 was necessary to find the correct fracture displacement for the notched specimens. After some trial and error with simulation of the notch R0.4 specimen, the fracture displacement was obtained with good accuracy using 0.01 % as the value of f_0, which is a very significant reduction from the initial value of 0.5 %. When simulating the smooth specimen with the new value of f_0, the reduction made the fracture

displacement way too large. Because fracture occured due to void volume reaching the critical value, the value of f_{cr} was reduced in order to correct this. The fracture displacement finally reached satisfying accuracy for $f_{cr} = 1$ %. Simulation of the notched specimens with R0.8 and R2.0 showed that these values gave accurate results for all the specimens.

While the notched specimens were used to calibrate f_0 and f_{cr} for W460E, they were mainly used for control of the results for W700E and W900E.

For all materials and specimens, the simulation results compared with the experimental data are shown in figure 4.8.

4.4 Determination of k_ω

In order to adjust the parameter k_ω that scales the influence of shear stress flow on the void growth rate, it was needed to re-simulate material tests where the stress state is such that the function $\omega(\sigma_{ij})$ is significantly larger than zero. Such stress states are obtained in e.g. shear stress tests (plane stress with $\sigma^* \sim 0$) and plane strain tests (near plane stress with $\sigma^* \sim 2/3$), as will be explained later. By performing such tests and doing inverse modeling it is possible to adjust the value of k_ω that gives the best prediction of the force-displacement-behavior and/or fracture displacement of those tests, given already adjusted hardening parameters and the void volume fraction parameters f_0 and f_{cr}.

Digital image correlation
Both the shear stress tests and the plane strain tests were subject to digital image correlation (DIC) analyses. This means that with a certain predetermined frequency, e.g. 1 Hz, a close-up picture was taken of the samples, which had been spray painted in order to attain a speckle pattern, and then after the tests the image series were analyzed to set up a certain mesh and coordinate system on the physical specimen in which the strain field was computed for each image. To verify the reliability of the performed simulations, the strain field from these DIC analyses was compared, visually and by means of the strain's order of magnitude, with the strain field from simulation results. Details about the DIC analysis method and the calculations of von Mises equivalent strain field can be found in [16].

4.4.1 Use of shear stress test simulations

The shear stress tests described in section 3.2.2 were simulated using a reduced integration solid element model with the LS–DYNA code. The geometry had been modeled earlier by Gaute Gruben [19] and was re-meshed by the authors. Since

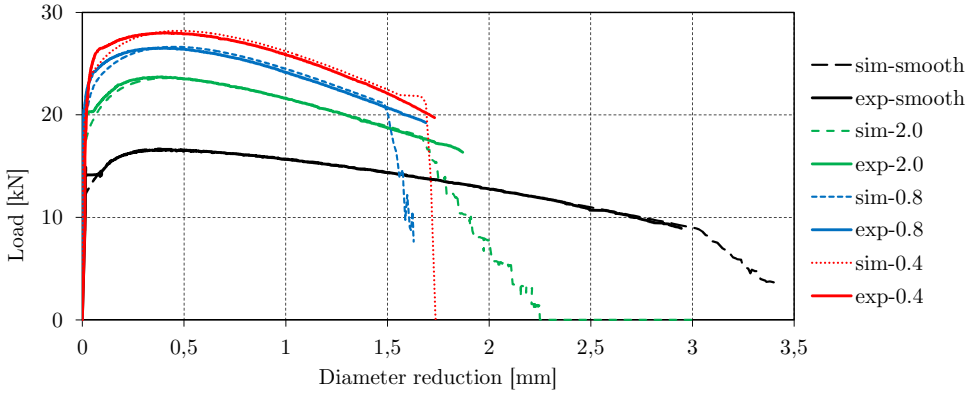

(a) W460E

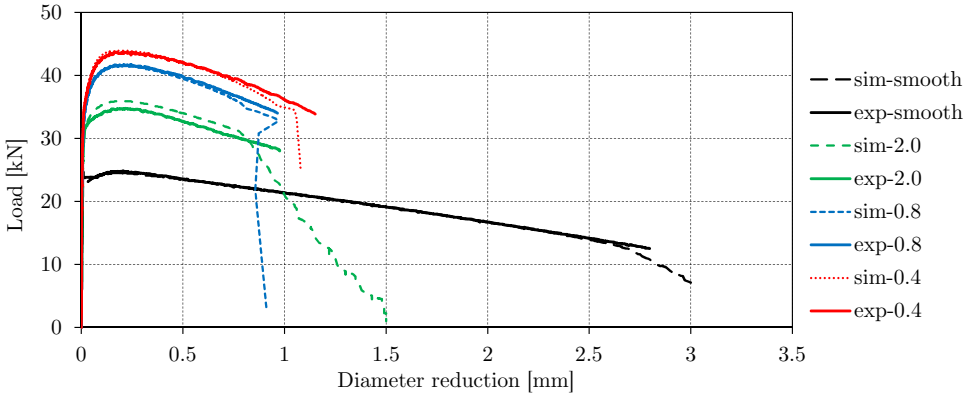

(b) W700E

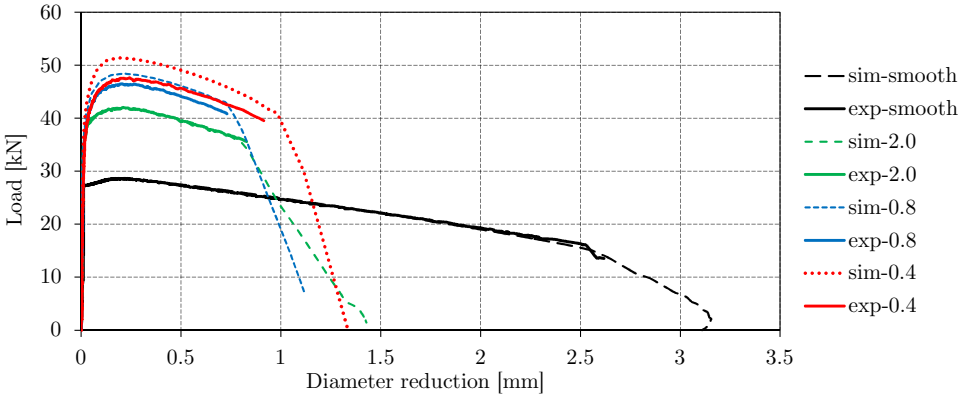

(c) W900E

Fig. 4.8: Results from smooth and notched specimen tensile test simulations using the calibrated material models. 'Simulation' and 'experiment' is abbreviated as 'sim' and exp' respectively and the notch radius r is indicated as -'r'

the area of interest on the test specimen is very small compared to many other tensile tests (only $\sim 5 \times 4$ mm) getting a proper resolution requires using very small elements. In addition to this the specimen is asymmetric such that one cannot model for instance only one quarter of it. To reduce the number of elements and computation time, the authors therefore desired to vary the element size in all three dimensions in the specimen. This was done [19] by making an unstructured mesh of most of the main geometry seen in figure 3.3, leaving only the shear deformation region in the middle of the specimen structured. Then, in order to vary the element size also in the thickness direction, the specimen was extruded to produce nine and three elements over the thickness in and outside of the shear deformation area, respectively, and bounded together with the tie algorithm "*CONTACT TIED NODES TO SURFACE" in LS–DYNA. The meshed specimen is shown in figure 4.9 and contains 23,070 elements in total and 5,576 elements in the shear deformation area.

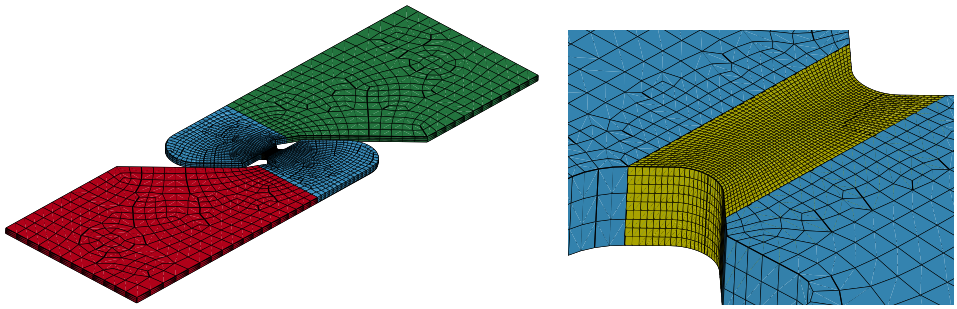

(a) Whole specimen (b) Shear deformation area

Fig. 4.9: Meshed shear stress specimen. Please note that the viewing angle is the same in (a) and (b).

In the simulations each of the two side-parts of the specimen was set to be rigid. This gave negligible deviation from simulations where the whole specimen was modeled with the calibrated modified Gurson material model. The test displacement could then simply be modeled by specifying each of the two rigid parts to move in the opposite direction of each other, each with half the displacement speed of the actual experiment (pulling only one of the edges). The extensometer displacement measured during the experiments were recovered as the relative displacement of the two rigid parts as the extensometer clamp contact in the experiment took place in the areas modeled as rigid in the simulations. The applied force in the simulations was measured in a cross section through the shear deformation area. A mass scaling factor of 10^{10} was applied, and it was controlled that the kinetic energy of the tension event never exceeded a fraction of 10^{-4} of the total energy.

Simulation results

The results from the shear stress test simulations varying only the parameter k_ω, are shown in figure 4.11. They show that the optimization of the k_ω value is straight forward, and that a fairly good reproduction of the shear stress test results can be achieved upon choosing that value. This is despite the fact that the stress level generally is a bit too high. This matter is discussed later on in section 4.6.

Comparison of the strain field calculated from DIC analyses with the strain field from the simulations showed good accordance, both with strain localization in a line slightly slanted relative to the tensional direction, but with a somewhat lower strain level in the simulation. This would suggest that the degree of localization is a bit too low in the simulations, which is a matter of discussed in section 4.6. Comparison between experiment and a simulation for the first W700E test (or "700–1") at an extensometer displacement of 1.6 mm is shown i figure 4.10.

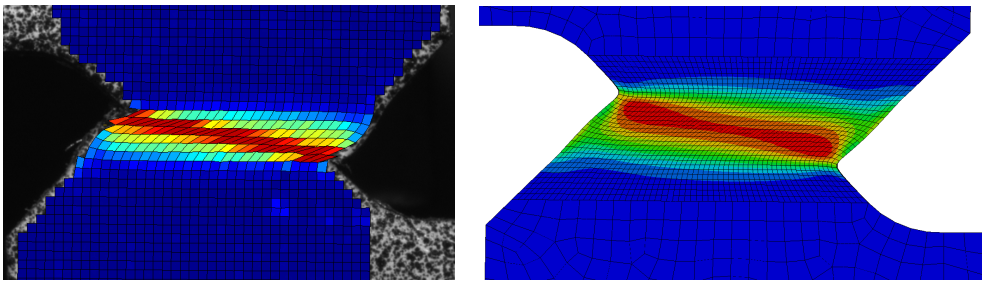

(a) DIC analysis (b) Simulation, $k_\omega = 2.0$

Fig. 4.10: DIC–simulation comparison of the strain field at 1.6 mm extensometer displacement for the W700E shear stress test. The coloring shows the level of equivalent strain, and the maximum values are 1.0 and 0.75 in the DIC analysis strain field and simulation strain field, respectively.

4.4.2 Use of plane strain test simulations

The plane strain test was modeled with 28,859 reduced integration solid elements. Due to symmetry only one eighth of the specimen was modeled, and most of this model geometry, or specifically the blue part as seen in figure 4.12, was modeled as elastic while the rest was modeled with the calibrated modified Gurson model. The border between the two parts was placed at the position of the extensometer clamps in the experiments, such that the extensometer displacement from the tests was recovered as the displacement of the mid node of this border.

Symmetry constraints was naturally applied in all three symmetry planes, such that only one edge of the specimen was constrained to move — in half the displacement speed from the experiment. This movement was applied at the very edge of the

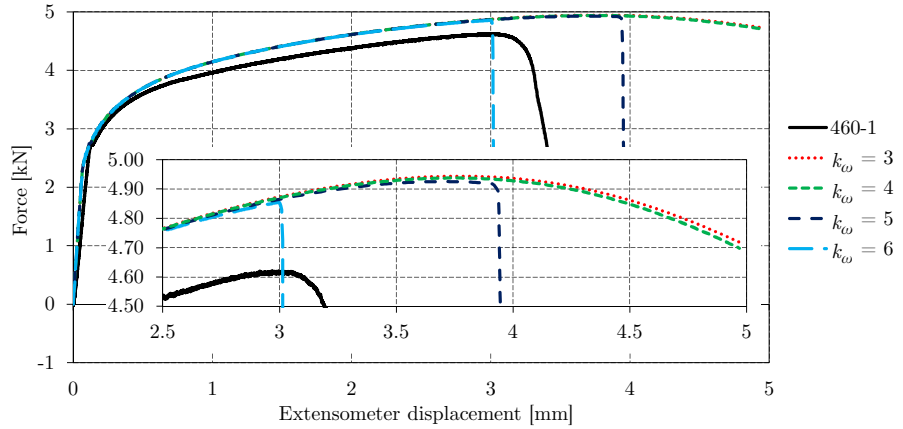

(a) W460E

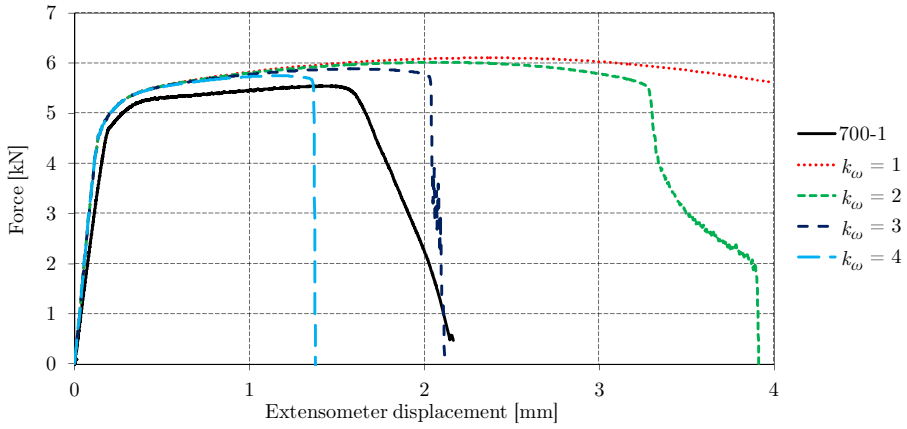

(b) W700E

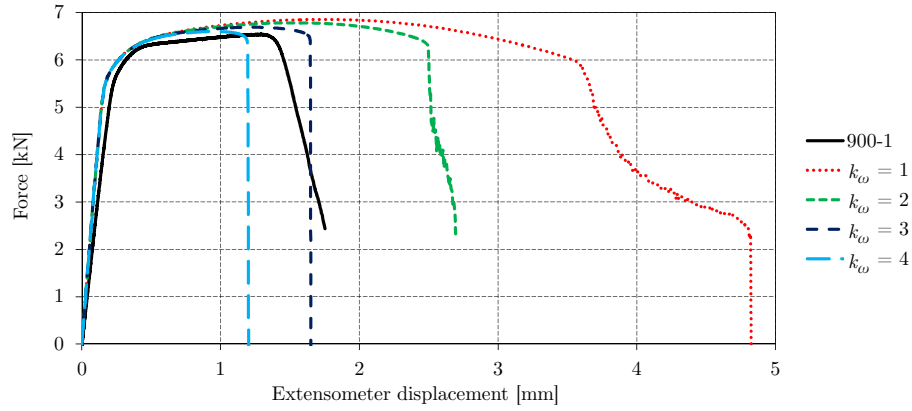

(c) W900E

Fig. 4.11: Results from shear stress test simulations using the calibrated material models.

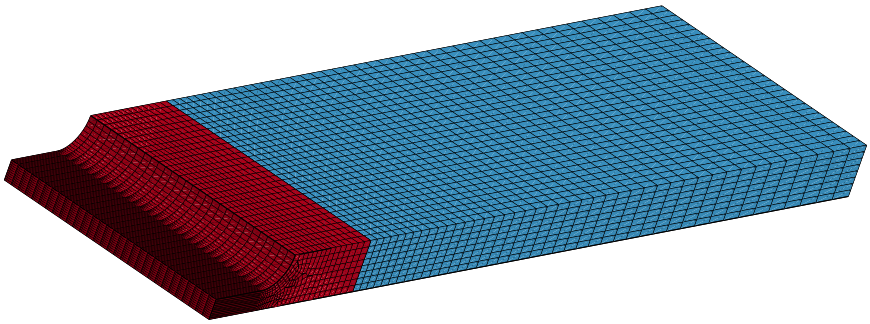

Fig. 4.12: Meshed plane strain specimen model, which in fact represents only one eighth of the real specimen as symmetry is applied in three dimensions.

specimen even though the specimen was clamped a few centimeters inwards from the edge in the experiment. This was assumed to have a negligible effect. The reaction force was measured as a "*SEGMENT FORCE" at the moving edge of the specimen.

Simulation results

The results from plane strain test simulations with the three steel alloys are shown in figure 4.13. Like the simulation results from the shear stress test simulations this figure shows fairly good accordance with the results, although the stress level is even a bit more too high. See section 4.6 for discussion. The reader is kindly asked to note that the fracture process is reproduced in a good manner for the W460E simulations, and although not evident from figure 4.13 this is most probably the case for W700E and W900E also. Here, namely, as also mentioned in section 3.3 and illustrated in figure 3.8, the clamping of the specimens was unfortunately made in a slightly slant manner (in all three tests for both W700E and W900E) causing the fracture mechanism in the specimens also to be slant/asymmetric. This caused a more brittle fracture and thus the 'fracture tail' of the experiment data in figure 4.13(a) is neither present in figure 4.13(b) nor 4.13(c). The same incident also took place in one of the W460E specimens (meaning that a total of seven out of nine specimens fractured slantly), which can be seen in figure 4.14 described below.

Like the shear stress tests the plane strain tests were subjected to DIC analyses, and strain field comparisons were performed in a similar manner, but comparison could only be done for the tests with the two symmetrically fractured W460E specimens. Comparison between a simulation and the first (asymmetric) and second (symmetric) W460E tension test performed is shown in figure 4.14. This figure shows that the flow pattern in the specimen is quite well reproduced — both in terms of appearance and level of equivalent von Mises strain.

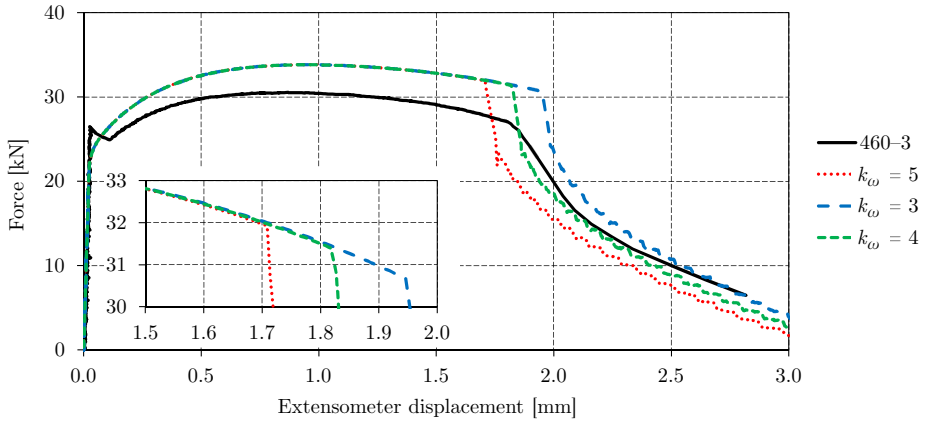

(a) W460E

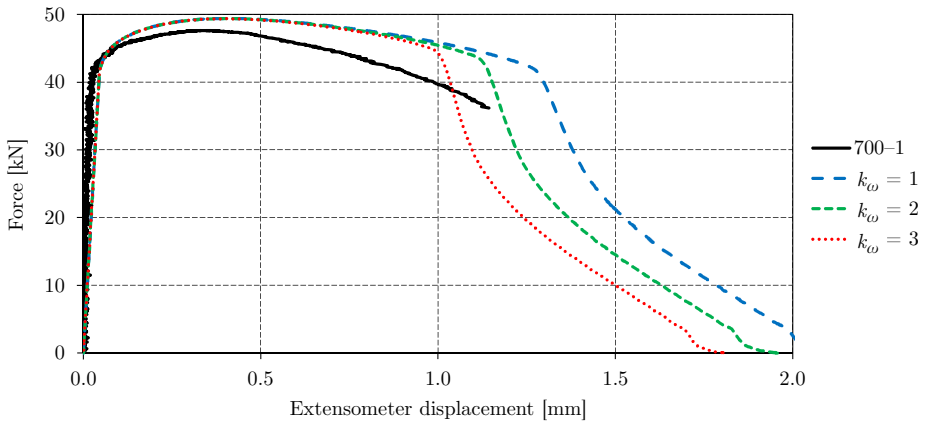

(b) W700E

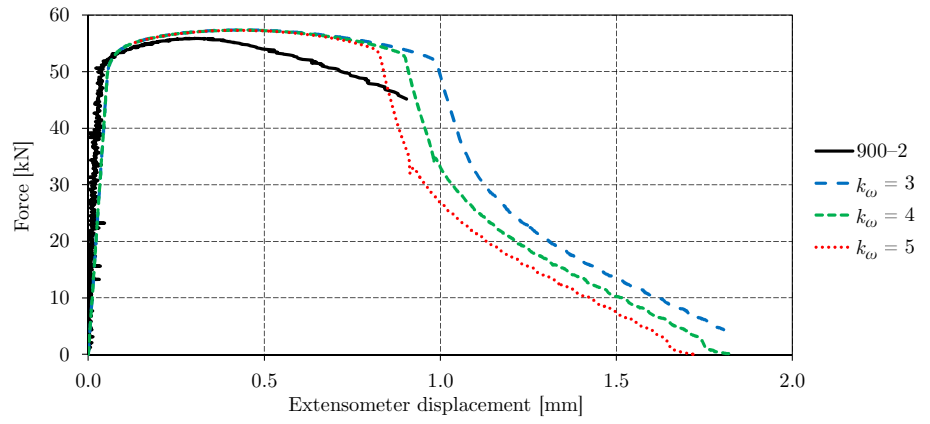

(c) W900E

Fig. 4.13: Results from plane strain test simulations using the calibrated material models.

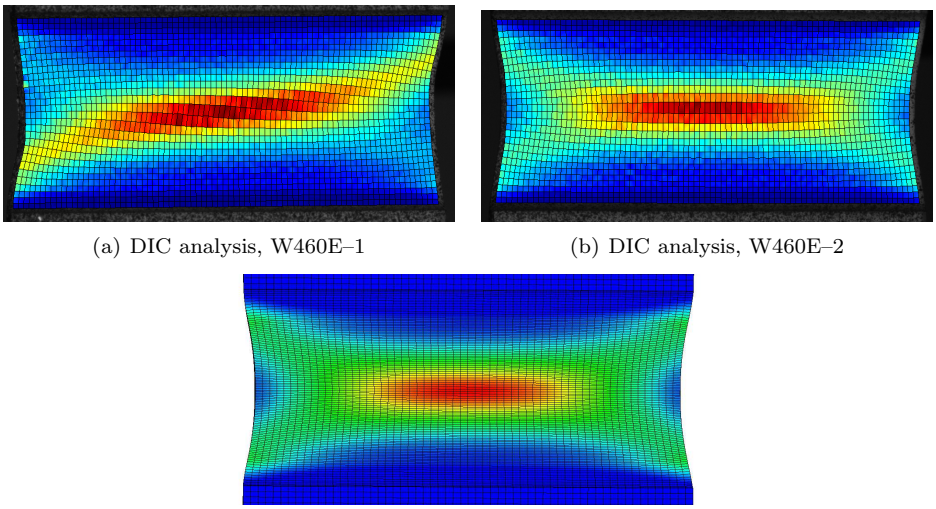

(a) DIC analysis, W460E–1

(b) DIC analysis, W460E–2

(c) Simulation

Fig. 4.14: DIC–simulation comparison of the strain field at 1.5 mm extensometer displacement for the first and second W460E plane strain test. The coloring shows the level of equivalent strain, and the maximum values are 0.5 in both the DIC analysis strain field and the simulation strain field.

4.5 Calibration results

In summary, inverse modeling of the axisymmetric tests have yielded the material parameters σ_0, Q_1, θ_1, Q_2, θ_2, f_0 and f_{cr} while the final parameter k_ω was determined through inverse modeling of the shear stress and plane strain tests. The obtained values for these parameters are summarized in table 4.2.

Table 4.2: Final extended Gurson model parameter values for W460E, W700E and W900E. For k_ω the first values optimizes the fracture displacement in shear stress test simulations while the values in parentheses optimizes it in plane strain test simulations.

	W460E	W700E	W900E
σ_0[MPa]	413.84	794.52	961
Q_1[MPa]	220	134.64	155
θ_1[MPa]	4678.1	4681.3	3000
Q_2[MPa]	491.53	2620.3	10000
θ_2[MPa]	395	253.7	170
f_0 [%]	0.01	0.5	0.5
f_{cr} [%]	1	25	18
k_ω	5.5 (4.0)	3.5 (2.0)	3.5 (4.0)

As can be seen from figures 4.11 and 4.13 there is a tendency for the optimum k_ω

value to be higher in shear stress than in plane strain for a given steel alloy. The optimal value is namely highest in shear stress for W460E and W700E, but for the most brittle steel considered, W900E, it is the opposite. This is clearly seen from the histogram in figure 4.15.

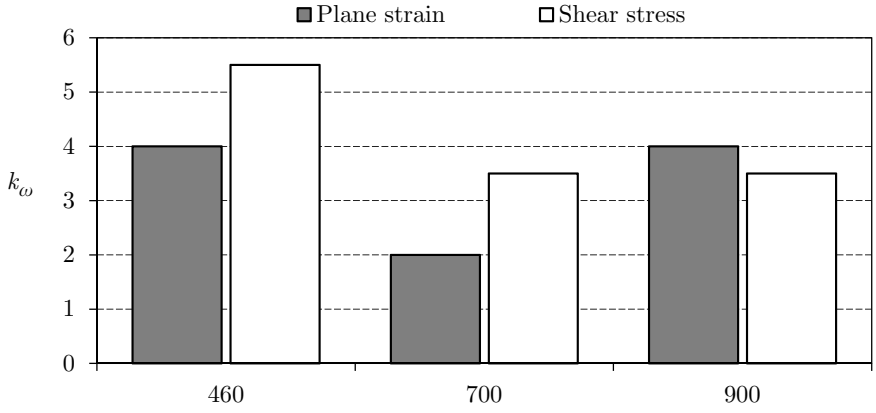

Fig. 4.15: Histogram of optimal k_ω values from plane strain and shear stress test simulations, respectively, showing that for the element size chosen there is needed a higher k_ω value for correct fracture displacement in in shear stress test simulations than plane strain test simulations.

4.6 Discussion

Void volume fraction

As discussed earlier the value of f_0 for W460E were initially set too high and had to be re-adjusted. The reason for this was that the ratio of equivalent stress to hydrostatic stress for some yielding elements became very low, i.e. they lost almost all their shear strength before the critical void volume fraction f_{cr} was reached. This led to a divergence of the iterative process determining the flow of these elements using the associated flow rule, i.e. the stress components update could not be calculated. These problems were first avoided by having LS-DYNA erode the elements which encountered this flow determination divergence. This was done at the time when the material model calibration were conducted, but was later removed as it seemed that the stress state causing the problem could be avoided. This element erosion criterion led to the fracture strain in all the W460E notched specimens being too small in the simulations compared to experimental data, as they witnessed a total loss of shear strength before the critical void volume fraction f_{cr} was reached.

A closer look at the simulations of the W700E specimens revealed that the tension simulations of notched specimens with R0.8 and R0.4 also witnessed element erosion due to total loss of shear strength, i.e. not reaching f_{cr}. Still, in contrast to the

first calibration of the W460E material model, the fracture strains coincided well with the experimental results, which led the authors to believe these results were fine. But later during penetration simulations, since this erosion criterion was not present at the time, the numerical problems caused by large void volume fraction prevented the completion of W700E plates for certain projectile velocities. This is explained in chapter 6.

The yield surfaces in figure 4.1 illustrates that σ_e/σ_m may be evaluated very close to zero if values of f in the range of 10-20 % is allowed. This means that f_{cr} probably should not have a value much higher than 10 %. It should nevertheless be noted that impact simulations for both W460E with $f_0 = 0.01$ % and $f_{cr} = 1.0$ %, and W900E with $f_0 = 0.5$ % and $f_{cr} = 18$ % were conducted without numerical problems, such that the range of possible void volume fraction parameter values is still wide and uncertain.

Mesh dependence

The mesh dependence of the shear stress test simulations are quite strong, cf. figure 4.16, and it is reasonable to assume that the same is the case for plane strain simulations. The authors assume that in reality the shear stress test localization zone is very small, e.g. on the scale of the grain size, such that for a good description of the test one might need an element size on the order of 1 μm or a number of $\sim 10^{10}$ elements for the shear stress test simulation specifically. It is also evident that the calibration of k_ω is strongly dependent of chosen element size, due to the fact that smaller element size makes the localization start sooner after the critical force level has been reached. Further, as one can see in figure 4.11, the speed of the fracture propagation in terms of displacement must be compromised in order to achieve a proper fracture displacement at the desired element size, indicating that the "true" value of k_ω (correct value for properly sized elements) is quite low — possibly below 1.

Due to the size of the area of interest in the shear stress test specimen the time step size became quite small, and hence the simulations became quite computationally demanding, when the element count exceeds $\sim 10^5$. Thus, no further mesh refinement was made in the mesh sensitivity study.

Yield surface

With proper strain hardening parameter values from the axisymmetric tests, the simulations of the shear stress and plane strain tests gave results that are showing too high stress levels compared to the experimental results. A reason for this may be the fact that the equivalent stress is here taken as von Mises equivalent stress, viz.

$$\sigma_e = \sqrt{\frac{1}{2}\Big[(\sigma_{\mathrm{I}} - \sigma_{\mathrm{II}})^2 + (\sigma_{\mathrm{II}} - \sigma_{\mathrm{III}})^2 + (\sigma_{\mathrm{IIII}} - \sigma_{\mathrm{I}})^2\Big]} = \sqrt{3J_2}$$

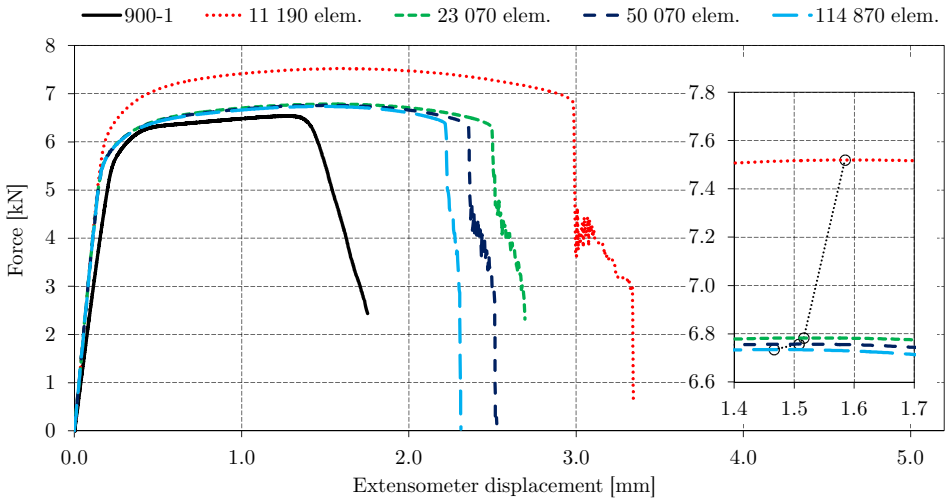

Fig. 4.16: Force-displacement curves from W900E shear stress test simulations with $k_\omega = 2$ and different element sizes. Clearly the mesh dependence of the simulation is strong and its convergence is slow. The critical force–displacement points are indicated to the right.

An alternative and most likely also more correct [10] measure that could be used is the equivalent stress resulting from the high-exponent yield criterion,

$$F = \left(\frac{1}{2} \left[|\sigma_\mathrm{I} - \sigma_\mathrm{II}|^m + |\sigma_\mathrm{II} - \sigma_\mathrm{III}|^m + |\sigma_\mathrm{III} - \sigma_i|^m \right] \right)^{1/m} - \sigma_Y = 0$$

where $m \geq 1$ determines the shape and contraction of the yield surface from the von Mises yield surface ($m = 2$) to the Tresca yield surface ($m \to \infty$).

When the material yields in the shear stress test, it has a stress state that approximately satisfies $\sigma_\mathrm{II} = -\sigma_\mathrm{I}$, while in the plane strain test the yielding stress state approximately satisfies $\sigma_\mathrm{II} = \sigma_\mathrm{I}/2$. In figure 4.17 the von Mises yield surface is plotted together with the high-exponent yield surface for $m = 6, 8, 20, 60$ assuming plane stress. It is evident from the figure that, given either of the two mention states of stress, the respective equivalent stress decreases for increasing value of m for both stress states. Please note the two arrows on the plane strain and shear stress lines that expresses the respective flow stress level differences between the different yield criteria, and that the differences in stress level for shear yielding are somewhat smaller than the differences in plain strain stress levels between the Tresca and the von Mises yield surfaces. This is namely also the case in the simulation-test-comparisons of plane strain and shear stress tests in figures 4.11 and 4.13. The observant reader would agree that this clearly suggests that a high exponent based yield surface for the Gurson model might be more correct than basing it on the von Mises yield criterion.

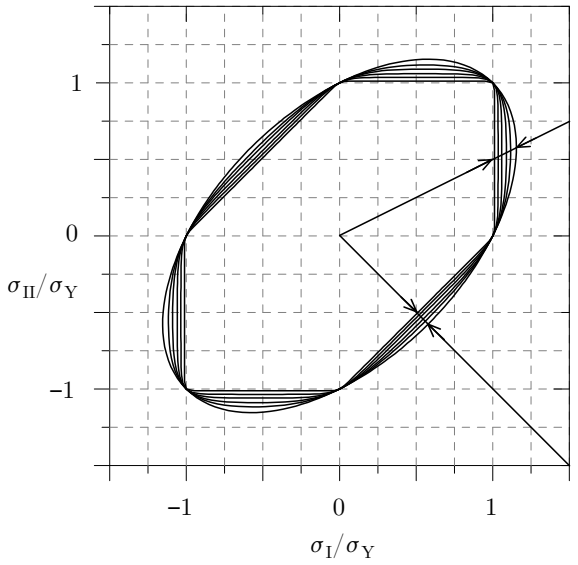

Fig. 4.17: High exponent yield surfaces for plane stress (i.e. $\sigma_{III} = 0$) with exponents $m = 2$ (von Mises yield surface), $m = 6$, $m = 8$, $m = 20$ and , $m = 60$. Note that the innermost yield surface of $m = 60$ is almost indistinguishable from the Tresca yield surface. The two lines plotted together with the yield surfaces are the requirements for tensional shear stress ($\sigma_{II} = -\sigma_I$) and tensional plane strain ($\sigma_{II} = \sigma_I/2$), respectively. Figure taken from [10].

Chapter 5
Impact tests

Penetration and perforation of steel plates exposed to ballistic impact have been studied by Sumita Dey [12], proceeding extensive work done by, amongst others, Tore Børvik, Odd Sture Hopperstad, Torodd Berstad and Magnus Langseth at SIMLab, cf. e.g. [5], [6], [7], [8]. Here, the smallest velocity in which target penetration is obtained, i.e. the *ballistic limit velocity*, is central as the dependencies on the target thickness, target hardness and projectile nose shape were studied. Impact experiment results were attempted reproduced in finite element simulations using the Johnson-Cook and Zerilli-Armstrong material constitutive relations. (Please see e.g. [12] for details on these constitutive relations). Both relations failed to predict the reduction in ballistic limit velocity for increasing target hardness with blunt projectiles, while test results for the other nose shapes were reproduced with satisfying accuracy.

The main objective with this thesis is to reproduce impact experiment results, with blunt nosed projectile, specifically, using the modified Gurson model, since earlier attempts in reproducing the steel alloy dependence on the ballistic limit velocity have not been successful. The test data used in this thesis was taken from experiments conducted by Dey [12].

It should be mentioned that in the studies of Dey [12] two different batches of W700E were considered, where impact tests using target plates made of the first batch were carried out by Børvik in 2001, while tests using the second batch was carried out by Dey in 2004. The results from material tests in this thesis are taken solely from the second batch, and since batch deviations in the mechanical properties occur the calibrated W700E material model can only be said to be valid for the second batch. Because of this it was chosen to entirely disregard impact test results from the first batch in this thesis.

5.1 Experimental setup

This section contains a brief summary of the main components in the experiments, namely the compressed gas gun, the equipment used for measurements, the projectiles and the target steel plates.

The main components of the gas gun were a 200 bar pressure tank, a purpose-built firing unit for compressed gas, a 10 m long smooth barrel of caliber 50 mm and a closed 16 m^3 impact chamber. This is shown i figure 5.1. The gas gun was designed to launch a 250 g projectile/sabot package to a maximum velocity of 1000 m/s when using helium as propellant.

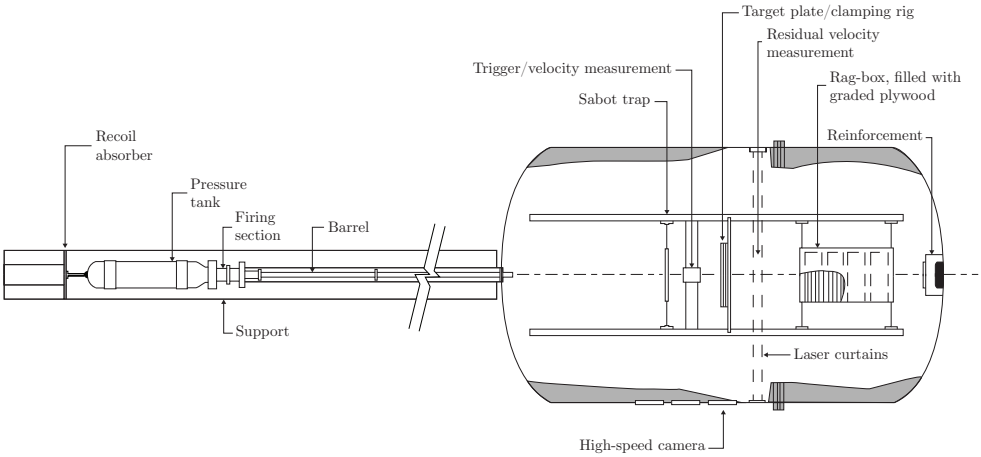

Fig. 5.1: The gas gun, firing barrel and impact chamber used by Dey [12]. Figure taken also from [12].

The initial velocity (v_i) was measured by a photocell system consisting of two identical light-barriers. The barriers consisted of LED light sources on the upper side of the projectile path and detectors on the lower side. When the projectile passed between the sources and detectors, the light was interrupted and signals were given to a nanosecond counter providing the velocity measurement data. A similar system was also used to measure residual velocities (v_{res}) for projectiles having perforated the target.

The high-speed camera system used consisted of an image converter camera and CCD camera. The image converter camera provided extremely fast shutter speeds, while the CCD camera provided digital images that were available immediately after testing. The system was fully computerized and capable of achieving frame rates from 2000 to 20,000,000 frames per second with exposure times down to 10 ns, and was used both for visualization and measurements. The camera system was set perpendicular to the projectile path in the target plane in order to record the projectile both before and after perforation. To reconstruct a 3D description of the penetration process, mirrors were used in some of the tests.

A more detailed explanation of test set up and implementation can be found in the aforementioned literature.

The original tests were performed with three different nose shapes; blunt, conical and ogival. In this thesis only blunt nosed projectiles is considered, due to problems with reproduction of results in numerical simulations, as mentioned above. The cylindrical projectiles were manufactured from Arne tool steel and the target steel plates were 12 mm thick and consisting of one of the steel alloys to be studied.

5.2 Test results

The results for all three materials are given in in table 5.1 and visualized in figure 5.2, where v_i denotes the projectile initial velocity and v_{res} denotes the residual velocity after perforation of the target plate. In addition to the values given in the table, for W900E a projectile with v_i of 165.1 m/s gave perforation, but the residual velocity was for some reason not measured, and it is therefore marked with a '–'. It is however still considered in the calculation of the ballistic limit velocity for W900E.

Table 5.1: Initial and residual projectile velocities from impact tests on W460E, W700E and W900E plates, taken from Dey [12].

W460E		W700E		W900E	
v_i	v_{res}	v_i	v_{res}	v_i	v_{res}
399.6	291.3	356.7	228	307.4	193.0
303.5	199.7	305.9	195	246.0	140.6
285.4	181.1	249.4	141	202.1	95.0
244.2	132.6	200.4	92	172.2	54.0
224.7	113.7	176.8	47	165.1	–
200.4	71.4	176.3	22	156.8	0.0
199.1	67.3	171.2	20		
189.6	43.7	165.1	0.0		
189.6	42.0	161.0	0.0		
189.2	40.1				
188.8	43.2				
184.3	30.8				
184.8	0.0				
181.5	0.0				
179.4	0.0				
177.3	0.0				
173.7	0.0				

Based on the results, the ballistic limit velocity v_{bl} was calculated for each steel alloy by taking the average of the highest velocity that did not give perforation and the lowest velocity that gave complete perforation of the target plate. The

ballistic limit velocity for each steel alloy is given in table 5.2. The results clearly indicate a decrease in v_{bl} for increasing yield strength, which is the key observation desired to reproduce using the modified Gurson model. This trend comes from the effect of increased degree of shear stress localization for increased material hardness, making the area absorbing the projectile's kinetic energy smaller and hence also the necessary work done in order to perforate the plate. There is not a linear relation between the difference in yield strength and ballistic limit though, as the decrease in v_{bl} relative to increase in yield strength between W460E and W700E is almost twice as big as between W700E and W900E.

Table 5.2: Experimentally determined ballistic limit velocities for W460E, W700E and W900E

alloy	v_{bl} [m/s]
W460E	184.6
W700E	168.2
W900E	161.0

Looking at the results in table 5.1 it is evident that the amount of data is quite scarce, to some extent for W700E but especially for W900E. This causes a considerable contribution to the uncertainty of the results, but some uncertainty also naturally arises from the nature of the experiment. High velocity projectiles are vulnerable to errors in both projectile shape and test setup, which can alter the projectile orientation at impact. Despite this, the data, with a few exceptions, show good consistency cf. figure 5.2.

The curves in figure 5.2 are fitted to the data points using an analytical model proposed by Recht and Ipson [29], which reads

$$v_{res} = a(v_i^p - v_{bl}^p)^{1/p}, \quad a = \frac{m_p}{m_p + m_{pl}}.$$

Here m_p is the mass of the projectile, m_{pl} is the mass of the plug that comes from the target plate when complete perforation occur, and both a and p are taken as parameters constituting the curve fit.

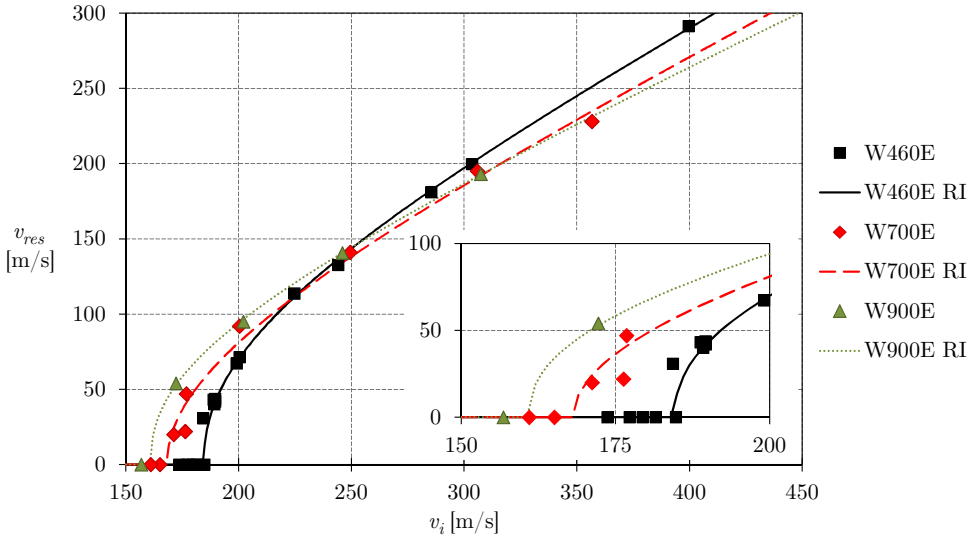

Fig. 5.2: Plot of residual velocities as a function of initial velocities of the blunt projectiles, taken from Dey [12], together with fitted RI curves

Chapter 6
Impact simulations

From the work with tension test data and inverse modeling of those tests it is possible to do the necessary modified Gurson model material modeling in order to simulate the perforation event of tool steel blunt projectiles penetrating armor plates of the three different Weldox® steel alloys studied. By performing a number of such simulations — varying the velocity v_i of the incoming projectile — the blunt projectile ballistic limit velocities for each alloy can be calculated, and based on these simulation results a conclusion can be made whether the modified Gurson model is able to reproduce the target plate stiffness dependency that is yielded by experiments [12], i.e. that the ballistic limit velocity decreases with increasing plate stiffness for blunt projectiles (i.e. in the event of penetration of the plate by perforation). This would namely indicate that the modified Gurson model is able to describe the increasing degree of stress localization for increasing stiffness in the steel plates.

6.1 Simulation setup

The geometry was modeled by reduced integration axial symmetric shell elements, i.e. in reality ring shaped elements with increasing radius (and volume for a given element area) with an increasing distance from the symmetry axis. This naturally constrains the perforation event to be axisymmetric, which is a reasonable assumption given that the projectiles were sufficiently axisymmetric in the experiments performed by Dey [12], but also saves quite a lot of computation time. The area (or in reality the cross sectional area) of the elements in the perforation area — or more precisely the smallest element size in the model which is in the area of the perforation event — was set to be ≈ 0.09 mm^2 which is consistent with the element sizes of the inverse modeling simulations performed to calibrate the modified Gurson model. The meshed geometry can be seen in figure 6.1 where symmetry is applied (horizontally).

The mesh consisted of 20,238 reduced integration elements where 19,438 was in the plate and 800 in the projectile. The mesh of the projectile is structured with quadratic shaped elements while the mesh of the target plate is structured in the impact zone, and biased such that the elements are smallest (and quite rectangular) in the shear zone and then unstructured with the number of elements across the thickness decreasing from 100 to 6 towards the restrained edge. See figure 6.1 for a

visualization of the mesh.

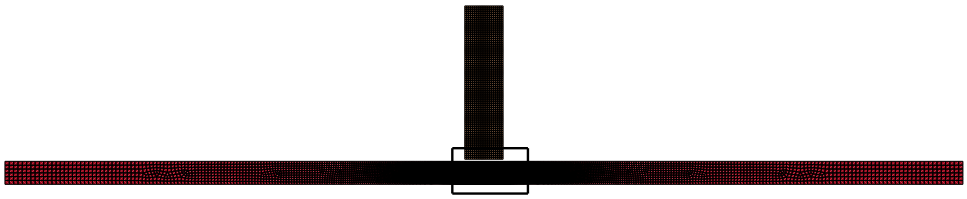

(a) Whole model. The contents of the rectangle is enlarged in (b).

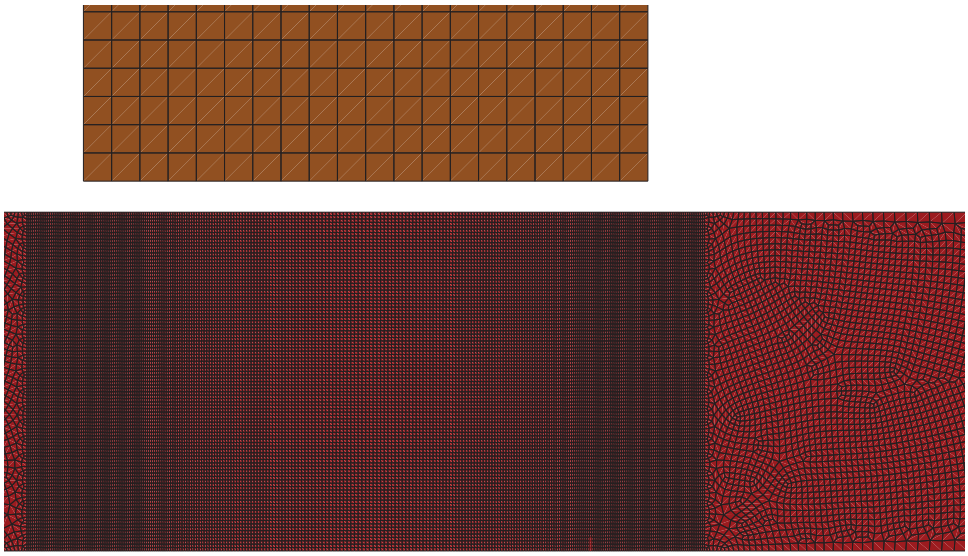

(b) Close up of the mesh inside the rectangle in (a)

Fig. 6.1: Mesh used in penetration simulations. Note that symmetry is applied here so that only half of the displayed elements are in the actual model and that they are all axisymmetric shell elements, i.e. in reality thin rings.

The hourglass control used in the penetration simulations was on Flanagan-Belytschko stiffness form and for contact the algorithm "*CONTACT 2D AUTOMATIC SINGLE SURFACE" in LS–DYNA was used, both with standard parameter values. The projectile was, in accordance with the work of Dey [12], modeled to be isotropically elastic – linearly plastic with a Young's modulus of 204 GPa, yield strength of 1.9 GPa and tangent modulus of 15 GPa.

The element erosion criteria used (in the UMAT implementation of the modified Gurson model) was

1) Critical void volume fraction f_{cr} cf. section 4.2 and 4.3,

2) Critical temperature T_{cr}.

As described in section 2.4 a temperature element erosion criterion is necessary for a model with a computationally realistic element size and the critical temperature was here set to approximately 90% of the melting temperature of steel, i.e. 1,620 K. [9] The heat that in fact causes some elements to reach that temperature and thus get eroded is due to the assumption of *adiabatic* heating, or more specifically that 90% of the plastic work done in an element is converted to heat that stays in that element. In other words we have used a Taylor-Quinney coefficient $\beta_{TQ} = 0.9$. The complete list of parameters used in impact simulations is given in table 6.1.

Table 6.1: Complete list of modified Gurson model parameters used in impact simulations. For k_ω it was used both the shear stress test adjusted values for each steel alloy in one set of simulations, and another set of simulations was carried out using $k_\omega = 0$ (i.e. the original Gurson model).

		W460E	W700E	W900E
σ_0	[MPa]	413.84	794.52	961
Q_1	[MPa]	220	134.64	155
θ_1	[MPa]	4678.1	4681.3	3000
Q_2	[MPa]	491.53	2620.3	10000
θ_2	[MPa]	395	253.7	170
f_0	[%]	0.01	0.5	0.5
f_{cr}	[%]	1	25	18
k_ω		5.5 (0)	3.5 (0)	3.5 (0)
ρ	[kg/m^3]	$7.85 \cdot 10^3$	$7.85 \cdot 10^3$	$7.85 \cdot 10^3$
E	[GPa]	210	210	210
ν		0.33	0.33	0.33
q_1		1.5	1.5	1.5
q_2		1	1	1
C		0.1	0.1	0.1
$\dot{\varepsilon}^P_{e,0}$		$5 \cdot 10^{-4}$	$5 \cdot 10^{-4}$	$5 \cdot 10^{-4}$
m		1	1	1
α	[K^{-1}]	$1.2 \cdot 10^{-5}$	$1.2 \cdot 10^{-5}$	$1.2 \cdot 10^{-5}$
β_{TQ}		0.9	0.9	0.9
c_T	[J/kg K]	452	452	452
T_{cr}	[K]	1620	1620	1620
T_m	[K]	1800	1800	1800
T_0	[K]	293	293	293

Finally it should be noted that impact simulations not only were performed with the calibrated *modified* Gurson model parameters as such, but that additionally

they all were performed with the *original* Gurson model, i.e. with $k_\omega = 0$ in order to potentially get an idea of the role that this parameter plays on the steel alloy dependence of the ballistic limit velocity.

6.2 Results

The perforation process

The simulations show unambiguously that approximately the first one fifth of the plate thickness is perforated due to elements reaching the critical temperature, while the rest of the plate thickness is perforated from damage (i.e. the critical void volume fraction being reached). These processes unfold simultaneously until at some point the temperature erosion stops and damage erosion continues throughout the perforation. For high impact velocities it was observed that the perforation path bifurcated, while at lower impact velocities the projectile made a clean cut of the target plate to produce a smooth plug.

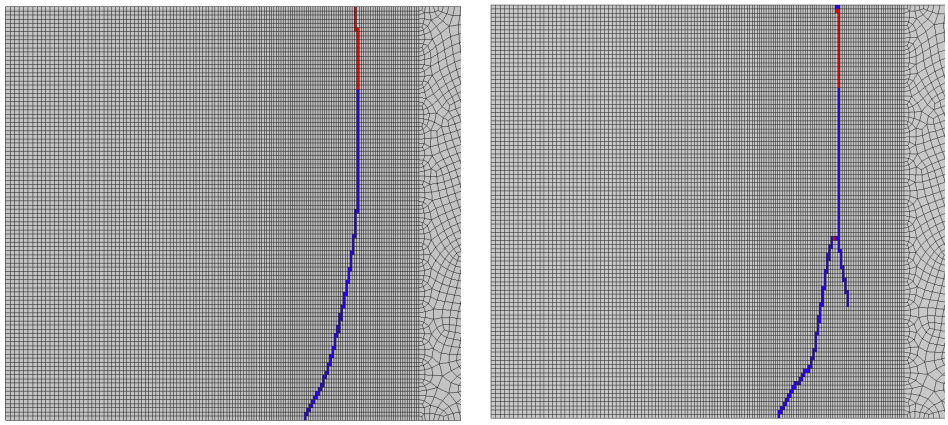

(a) $v_i = 163$ m/s (b) $v_i = 250$ m/s

Fig. 6.2: Element erosion pattern from W900E penetration simulations shown on the initial mesh configuration. Elements eroded from reaching the critical temperature are colored red while elements eroded from reaching the critical void volume fraction are colored blue.

The perforation process is further visualized in figure 6.3 where simulation *fringe plots* of the void volume fraction is displayed at four different times during perforation of a W900E plate. Here it can be seen that, during the very first moments after impact [6.3(a)], the void volume fraction f is reduced to zero from the initial void volume fraction $f_0 > 0$ in the near impact area of the plate. Further on there is a shear zone being localized before the perforation takes place [6.3(b)]. The fracture then propagates through the plate thickness [6.3(c)], actually both by elements reaching critical temperature *and* elements reaching the critical void volume

fraction. Finally the produced plug travels through the fractured plate [6.3(d)].

Projectile residual velocity

In order to recover the projectiles' residual velocity from simulations the velocity of the front and rear end of the projectiles were saved at a high frequency and then plotted as a function of time. A such plot is shown in figure 6.5, where one can see that the projectile starts to oscillate elastically after impact. The residual velocity was found in each simulation by finding the duration of the perforation process and taking the average of the highest crest and the lowest troughs of the two waves (e.g. as displayed in figure 6.5) in the first couple of wavelength after the perforation process had finished. Repeating this process for simulations with different initial projectile velocities, values of k_ω and target plate steel yielded the data visualized in figure 6.4 (residual projectile velocity as a function of initial projectile velocity), and the final ballistic limit velocities given in table 6.2 and visualized in figure 6.6. Figure 6.4 shows that the degree of reproduction of experiment data is varying, but that the projectile initial velocity dependence on the projectile residual velocity is fairly the same as in experiments. Figure 6.6 shows that the correct steel alloy dependence on the ballistic limit for the blunt projectile is recovered from simulations with $k_\omega = 0$, and not from simulations using the adjusted values. This matter is of utmost importance and is further discussed in section 6.3.

Table 6.2: Ballistic limit velocity v_{bl} results for W460E, W700E and W900E simulations and experiments visualized in figure 6.6. The data from simulations with the modified and the original Gurson model are compared with experiments and simulation results taken from Dey [12]. For the latter we have taken the results obtained with the most similar mesh (Dey's "120" mesh) and with the Cockroft–Latham ('CL') and the Johnson–Cook ('JC') damage model, respectively.

	W460E	W700E	W900E
experiments	184.6	168.2	161.0
simulation	151.7	163.0	165.7
sim., $k_\omega = 0$	184.2	183.4	172.0
Dey, CL	205.0	209.7	219.2
Dey, JC	189.3	211.0	214.1

6.3 Discussion

All of the parameters of the modified Gurson material model was, with one exception, calibrated using simulations with shell elements. This one exception is k_ω, which was determined from simulations using solid elements. Please note also that the impact simulations themselves were done using shell elements. The fact that results from simulations using a material model with $k_\omega = 0$ gave a correct material dependency on the ballistic limit velocity, and not using k_ω values calculated

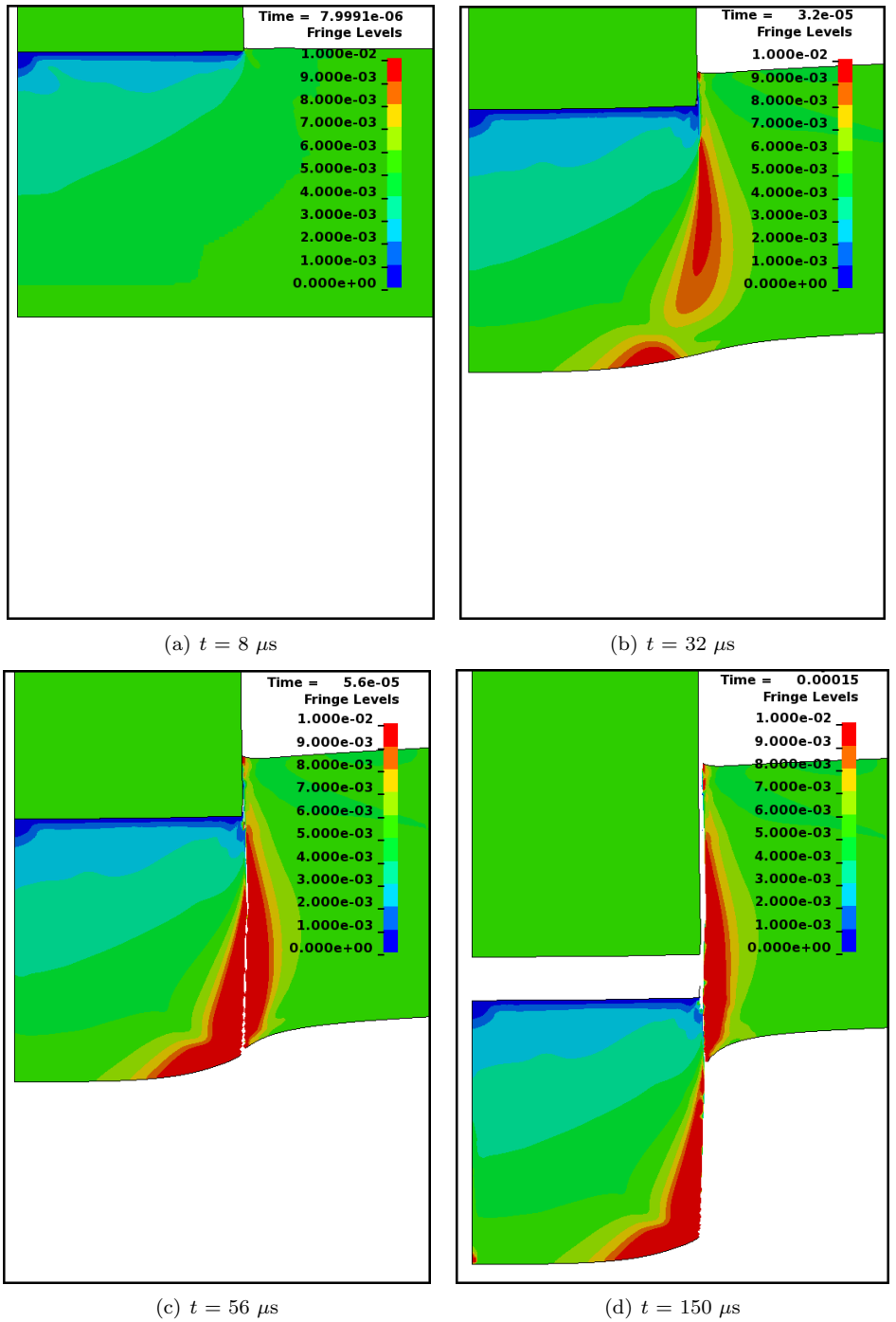

(a) $t = 8\ \mu s$ (b) $t = 32\ \mu s$

(c) $t = 56\ \mu s$ (d) $t = 150\ \mu s$

Fig. 6.3: Simulation visualization of the perforation of a W900E target plate by a projectile with an initial velocity of 175 m/s. The color visualizes the void volume fraction f and the left hand side of each figure is axis of rotational symmetry.

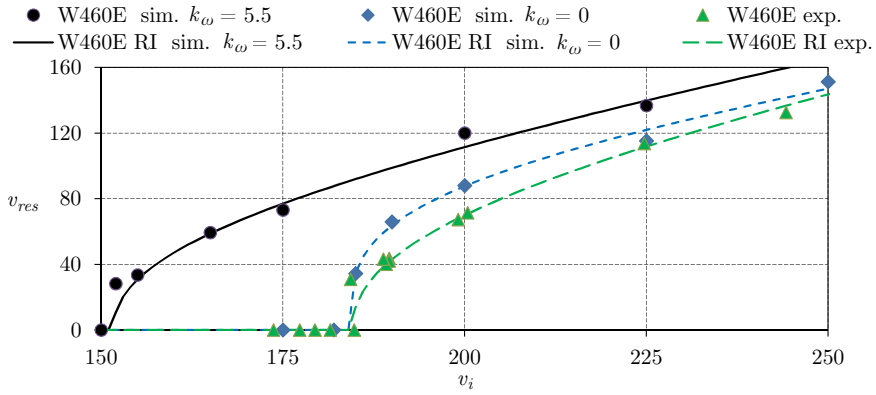

(a) W460E

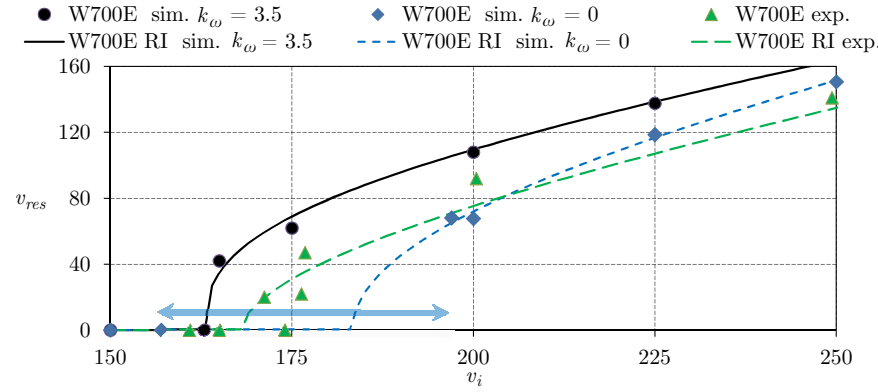

(b) W700E

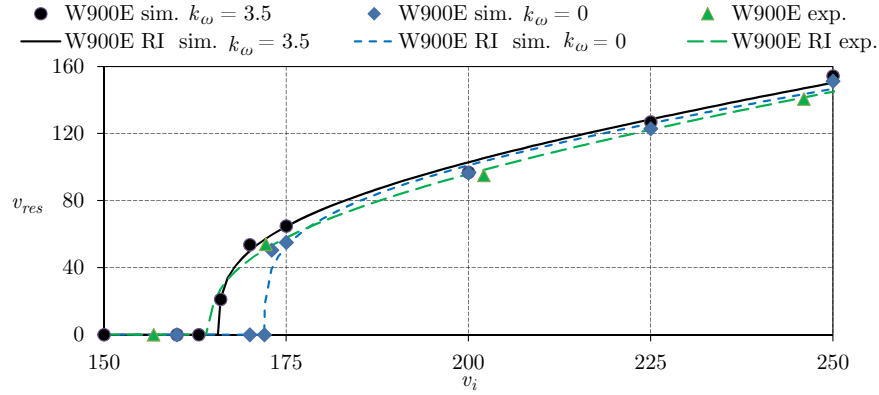

(c) W900E

Fig. 6.4: Residual velocities as a function of respective initial velocities for W460E, W700E and W900E penetration simulations and experiments ('sim.' denotes simulations and 'exp.' denotes experiments). The blue arrow along the abscissa in 6.4(b) represents the interval of v_i that the LS–DYNA UMAT could not conduct complete simulations

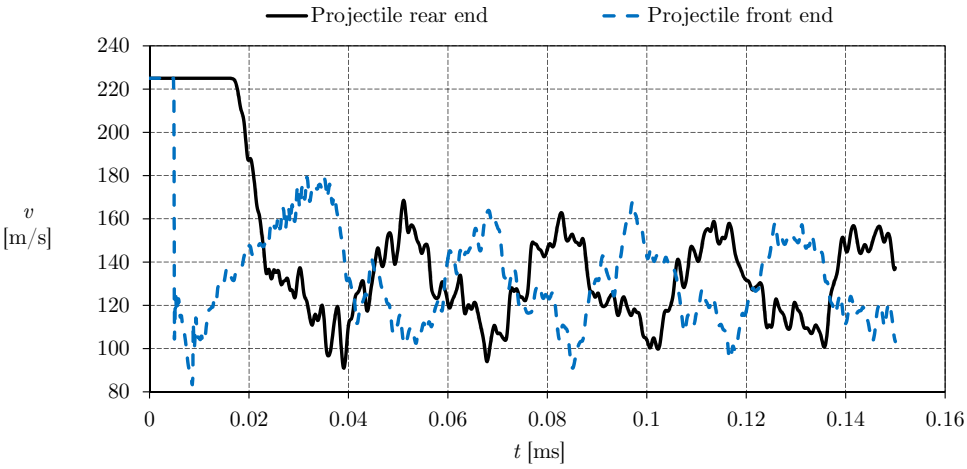

Fig. 6.5: Velocity of a W900E projectile's frond and rear end as a function of time during penetration. Evidently the incoming velocity of the projectile was 225 m/s in this particular simulation.

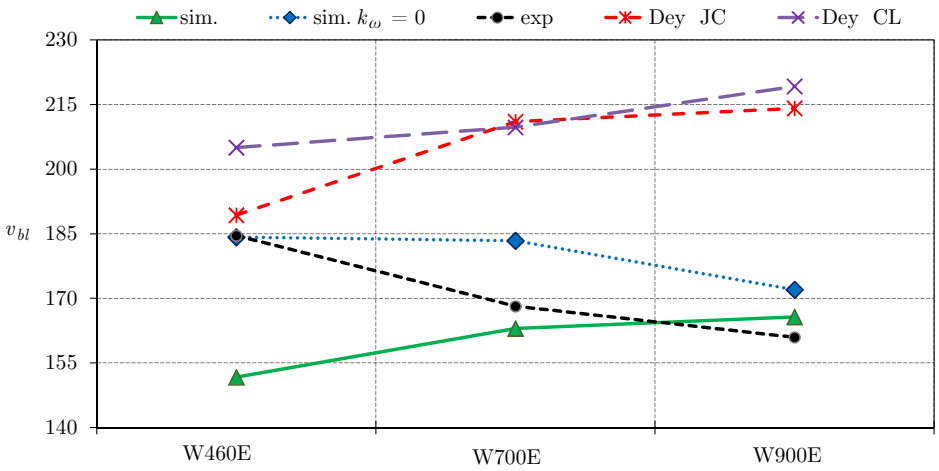

Fig. 6.6: Ballistic limit velocity v_{bl} results for W460E, W700E and W900E simulations and experiments

from simulations with solid elements, can cast some doubt on whether the modified Gurson model is able to predict the dependence of shear stress localization on the material hardness in a satisfying manner. It be noted, however, that this particular dependence might not be so clear if it had been possible to perform a complete set of impact simulations for the W700E target plate with $k_\omega = 0$, since the lack of data on the interval 157 – 197 m/s (cf. figure 6.4(b)) greatly increases the uncertainty of the ballistic limit velocity for the *original* Gurson model W700E material. There may be other reasons for the negative influence on the accuracy of the results from introducing k_ω in the material model, so that there should probably have been done a further verification of the values for k_ω, especially in simulation models using shell elements. All in all though, the results made from both the original and modified Gurson model show a fairly good consistency with experiments. In fact they can both be said to reproduce the approximate magnitude of the ballistic limit velocity better than Johnson–Cook and Zerilli–Armstrong simulations performed by Dey [12] as shown in figure 6.5.

The fracture pattern in a $k_\omega = 0$ (i.e. original Gurson model) simulation is slightly different from the pattern in a corresponding modified Gurson model simulation. The most important difference is that the fracture evolves a bit more slowly with the original Gurson model, and that temperature erosion of the uppermost part of the target plate is not continuous. This means that in between elements eroded due to temperature there are elements that were eroded due to the critical void volume fraction being reached. This is seen in figure 6.7(b).

The mesh sensitivity of the perforation event was not studied in this thesis. The use of shell elements and a coupled damage model causes no mesh convergence to be obtained. This implies that the material model calibration is mesh dependent, so the question is really whether a mesh refinement *and* a material model re-calibration would have had an effects. It is known from the mesh sensitivity study of the shear stress test (cf. figure 4.16) that the increased degree of localization due to mesh refinement causes the optimal value of k_ω to decrease. This could perhaps cause a less intense effect of shear on the void volume fraction and thus, possibly, have a positive effect on the steel dependence on the ballistic limit velocity. A mesh refinement would also have an effect on the temperature erosion mechanism, that is — make it *more* intense, since the localization length scale would be smaller and hence less elements would be heated dramatically.

It should further be mentioned that there has neither been done studies on the sensitivity of the critical temperature used in the simulations. This temperature was here set to 90% of the melting temperature of steel taken as 1,800 K, i.e. 1,620 K, due to experience of the supervisors [9], [21]. But this experience does not come from work with the modified Gurson model specifically, and it might be that this critical temperature is more important here than when using other constitutive relations and damage models. In fact, the correct reproduction of steel dependence

on the ballistic limit velocity might be based on the critical temperature not being high enough to ensure a continous temperature erosion fraction of the uppermost part of the target plate, as seen in figure 6.7.

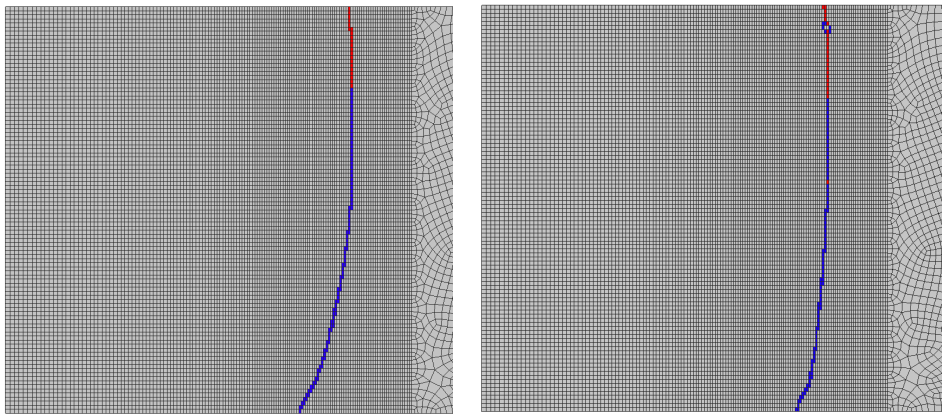

(a) $v_i = 163$ m/s, $k_\omega = 4.0$ (b) $v_i = 175$ m/s, $k_\omega = 0$

Fig. 6.7: Element erosion patterns from W900E penetration simulations shown on the initial mesh configuration. Elements eroded from reaching the critical temperature are colored red while elements eroded from reaching the critical void volume fraction are colored blue. In the $k_\omega = 0$ case the simulation ballistic limit velocity was 172.0 m/s while in the simulation with the modified Gurson model (i.e. with the correct adjusted value of $k_\omega = 4.0$) the simulation ballistic limit velocity was 165.7 m/s. One can see that the fracture mechanism is different in the two cases by looking at the upper part of the fracture paths.

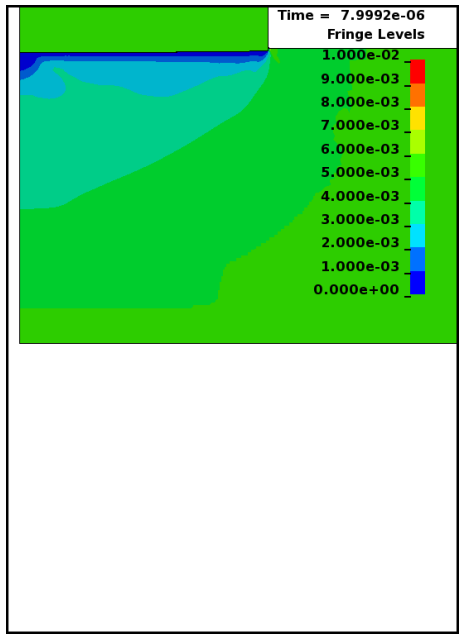

(a) $t = 8$ μs

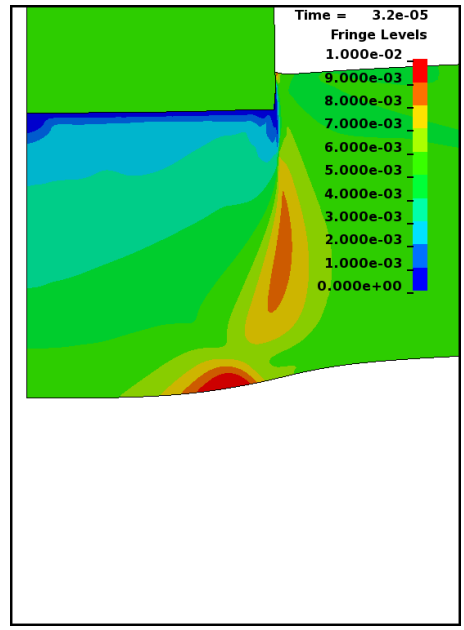

(b) $t = 32$ μs

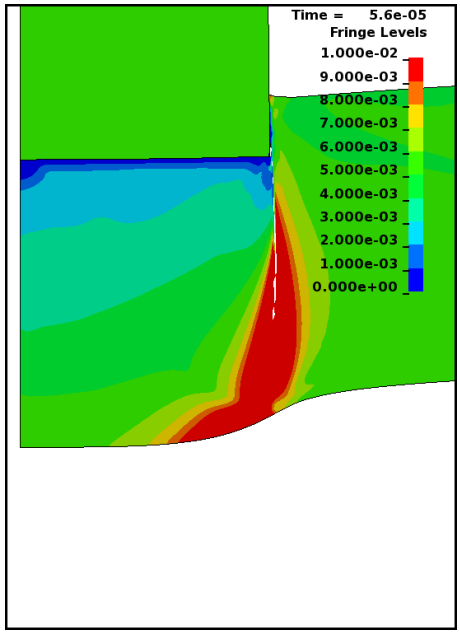

(c) $t = 56$ μs

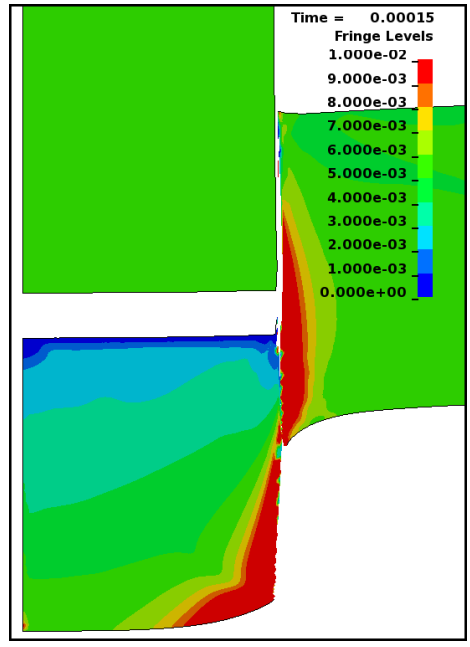

(d) $t = 150$ μs

Fig. 6.8: Simulation visualization of the perforation of a W900E $k_\omega = 0$ target plate by a projectile with an initial velocity of 175 m/s. The color visualizes the void volume fraction f and the left hand side of each figure is axis of rotational symmetry.

Chapter 7
Concluding remarks

Calibration of the modified Gurson model

- Using the finite element model LS–DYNA the modified Gurson model has proved to be quite possible to calibrate in the work with three different steel alloys, using material test results and inverse modeling. Inverse modeling with manual parameter adjustments has proved to constitute a reliable calibration method. Such calibrations have yielded material models well capable of reproducing the force–displacement behavior observed in the material tests performed.

- Variations in the value of f_0 in the modified Gurson model influences the plastic hardening of the material, and has to be accounted for when adjusting work hardening parameters.

- A modified Gurson material model with a relatively large value for f_0, which creates a large void volume fraction when subjected to stress, may be problematic in numerical simulations because of total loss of shear strength when the ratio of equivalent stress to hydrostatic stress becomes small. An erosion criterion may be introduced to remove elements experiencing this stress state, but a more reliable solution is to pick a value of f_0 small enough such that elements are only eroded when the void volume fraction reaches f_{cr} (when other erosion criteria is not present). This fact has to be taken direct care of since a pair of f_0 and f_{cr} values could be used to describe a behavior very similar to that of a different pair with a quite different magnitude of void volume fraction.

- Simulation results for both shear stress test and plane strain test specimens, using material parameters valid for simulation of axisymmetric tests, both exhibit material behavior that is too stiff. In fact, the plane strain test stress level is a bit more too high than the shear stress test stress level, and this clearly suggests that use of a high exponent based yield criterion should be used instead of the von Mises based yield criterion.

Simulation of impact using the modified Gurson model

- The dependence on the blunt projectile ballistic limit velocity of the target plate steel strength seen in experiments, i.e. that the ballistic limit velocity *decreases* with increasing steel strength, is recovered using the original Gurson model. The modified Gurson model predicts ballistic limit velocities of the

same order of magnitude as the original Gurson model, but fails to exhibit the correct target plate strength dependence. This dependence is in fact seen to be quite similar to that of Johnson–Cook and Zerilli–Armstrong constitutive relations.

Chapter 8
Further work

In the work with this thesis the authors were not able to fully reproduce experimental results from ballistic impact using blunt nose projectiles on Weldox® steel plates with decreasing ballistic limit velocity for increasing yield strength in the target plate using the extended Gurson model in numerical simulations. Further work can be done in order to get better a better perspective on the capabilities of the modified Gurson model, and hopefully verify that it is able to reproduce the correct target plate strength dependence on the ballistic limit velocity in impact simulations with blunt nosed projectiles. Specifically we suggest the following.

- The value of f_0 being 50 times as high for W700E and W900E as for W460E gave satisfying results for all simulations of material tests performed in this thesis, but the difference seems unrealistic from a physical point of view, as the three alloys are quite similar. Further investigating and adjusting values for f_0 and f_{cr} of the same magnitude for W700E and W900E as for W460E could possibly create a more reliable basis for comparison of the alloys, or more importantly, a more reliable basis for the evaluation of the modification of the Gurson model for shear stress failure proposed by Nahshon and Hutchinson [26].
- Implementation of a high-exponent-based yield criterion instead of the von Mises based criterion used in this thesis with the modified Gurson model would hopefully make the model more capable of predicting proper material behavior, such as in shear stress and plane strain tests.
- Reproducing the shear zone in the ballistic impact experiments accurately in numerical simulation models require a very small element size. When using element erosion to represent fracture in FEM simulations, the element size in the simulation model represents the width of the physical crack with in the experiments, which in reality seems to be extremely small. Due to time constraint and the amount of computational time needed becoming very large due to a possible moderate element size reduction, a mesh sensitivity study of the impact simulations was not performed. A comprehensive study, with material calibration for different element sizes, could be performed in order to determine a suitable element size when considering both material model performance and computational time.
- The critical temperature value used in the temperature element erosion criterion in the impact simulation has not been subjected to neither calibration

nor sensitivity studies. A material test to verify, or possibly improve, the value used would make the material model more reliable.

- In order to further study the results from material tests, a more comprehensive utilization of digital image correlation (DIC) could be made in order to recover data such as fracture strains.
- A method to verify values of k_ω calculated from solid element simulations being used directly in simulations with shell elements could ensure better performance of the material model in impact simulations.

Bibliography

[1] G.I. Barenblatt,
The mathematical theory of equilibrium cracks in brittle fracture, Advanced Applied Mechanics **7** (1962) 55–129

[2] R. Becker,
Ring fragmentation predictions using the Gurson model with material stability conditions as failure criteria, International Journal of Solids and Structures **39** (2002) 3555-3580

[3] R. de Borst,
Damage, Material Instabilities, and Failure, Encyclopedia of Computational Mechanics, Volume 2: Solids and Structures, Wiley 2004.

[4] P. W. Bridgman,
Transactions of the American Society for Metals **32** (1944) 553.

[5] T. Børvik, O.S. Hopperstad, T. Berstad, M. Langseth,
Computational model of viscoplasticity and ductile damage for impact and penetration, European Journal of Mechanics and Solids **20** (2001) 685-712

[6] T. Børvik, M. Langseth, O.S. Hopperstad, K. A. Malo,
Perforation of 12 mm thick steel plates by 20 mm diameter projectiles with flat, hemispherical and conical noses. Part I : Experimental study, International Journal of Impact Engineering **27** (2002) 19-35

[7] T. Børvik, O.S. Hopperstad, T. Berstad, M. Langseth,
Perforation of 12 mm thick steel plates by 20 mm diameter projectiles with flat, hemispherical and conical noses. Part II : Numerical simulations, International Journal of Impact Engineering **27** (2002) 37-64

[8] T. Børvik, O.S. Hopperstad, T. Berstad, K. A. Malo,
Effect of target thickness in blunt projectile penetration of Weldox 460 E steel plates, International Journal of Impact Engineering **28** (2003) 413-464

[9] T. Børvik,
Personal communications 2011/2012, Department of Structural Engineering, Norwegian University of Science and Technology

[10] T. Børvik, O.S. Hopperstad,
Lecture Notes in TKT4135 Mechanics of materials, Department of Structural Engineering, Norwegian University of Science and Technology (2010)

[11] D. R. Curran,
Simple fragment size and shape distribution formula for explosively fragmenting munitions, International Journal of Impact Engineering **20** (1997) 197-208

[12] S. Dey,
High-strength steel plates subjected to projectile impact, Department of Structural Engineering, Norwegian University of Science and Technology (2004)

[13] G. E. Dieter
Mechanical Metallurgy. London: McGraw-Hill Book Company; 1988

[14] D. C. Drucker,
A definition of stable inelastic material, Journal of Applied Mechanics **26** (1959) 101-106

[15] D.S. Dugdale,
Yielding of steel sheets containing slits, Journal of the Mechanics and Physics of Solids **8** (1960) 100–108

[16] E. Fagerholt,
Field Measurements in Mechanical Testing Using Close-Range Photogrammetry and Digital Image Analysis, Department of Structural Engineering, Norwegian University of Science and Technology (2012)

[17] D.M. Goto, R. Becker, T.J. Orzechowski, H.K. Springer, A.J. Sunwoo, C.K. Syn,
Investigation of the fracture and fragmentation of explosively driven rings and cylinders, International Journal of Impact Engineering **35** (2008) 1547-1556

[18] M. Gromada, G. Mishuris, A. Öchsner,
Correction Formulae for the Stress Distribution in Round Tensile Specimens at Neck Presence, chapter 2, Springer; 2011

[19] G. Gruben,
Personal communications 2011/2012, Department of Structural Engineering, Norwegian University of Science and Technology

[20] A. L. Gurson,
Continuum theory of ductile rupture by void nucleation and growth: Part I — Yield criteria and flow rules for porous ductile media, Journal of Engineering Materials and Technology **99** (1977)

[21] O. S. Hopperstad,
Personal communications 2012, Department of Structural Engineering, Norwegian University of Science and Technology

[22] J. Koplik, A. Needleman,
Void growth and coalescence in porous plastic solids, International Journal of Solids and Structures **24** (1988) 835-853

[23] G. LeRoy, J. Embury, G. Edwards and M. F. Ashby,
A model of ductile fracture based on the nucleation and growth of voids, Acta Metallurgica **29** (1981) 1509-1522

[24] W. Lode,
The influence of the intermediate principal stress on yielding and failure of iron, copper and nickel, Zeits. Eng. Math. Mech. **5** (1925) 142

[25] N. F. Mott,
Investigation of the fracture and fragmentation of explosively driven rings and cylinders, Proceedings of the Royal Society of London. Series A, Mathematical and Physical **108** (1947) 300-308

[26] K. Nahshon, J.W. Hutchinson,
Modification of the Gurson model for shear failure, European Journal of Mechanics and Solids **27** (2008) 1-17

[27] K. L. Nielsen, J.W. Hutchinson,
Cohesive traction-separation laws for tearing of ductile metal plates, International Journal of Impact Engineering (2011)

[28] A. Pandolfi, P. Krysl, M. Ortiz,
Finite element simulation of ring expansion and fragmentation: The capturing of length and time scales though cohesive models of fracture, International Journal of Fracture **95** (1999) 279-297

[29] R.F. Recht, T.W. Ipson,
Ballistic perforation dynamics,

Journal of Applied Mechanics **30** (1963) 384-390

[30] K.L. Roe, T. Siegmund,
An irreversible cohesive zone model for interface fatigue crack growth simulation, Engineering Fracture Mechanics **70** (2003) 209-232

[31] SSAB on the Word Wide Web,
http://www.ssab.com/en/Brands/Weldox/Products1/
Weldox – Products, accessed January–June, 2012

[32] V. Tvergaard,
Influence of voids on shear band instabilities under plane strain conditions, International Journal of Fracture **17** (1981) 389-407

[33] E. Voce,
Journal of the Japan Institute of Metals **74** (1948) 537-562

[34] Z. Xue, M.G. Pontin, F.W. Zokb, J.W. Hutchinson,
Calibration procedures for a computational model of ductile fracture, Engineering Fracture Mechanics **77** (2010) 492-509

[35] C. D. Øien,
Validation of a modified Gurson model LS–DYNA user material sub-routine, Project report, Norwegian University of Science and Technology, Faculty of Natural Sciences and Technology (2011)

Appendix A
MATLAB script for integration of the modified Gurson model constitutive equations

```
% Assumptions:
%     - Plane stress (sigma1>0 sigma2=0 sigma3<0) for |triAx|<1/3.
%     - Axisymmetric stress (sigma1>sigma2=sigma3 or sigma1=sigma2>sigma3)
%           for |triAx|>1/3.

clear all
close all
clc

% Material parameters
A=1250e6;                   % Power law hardening
B=200e6;
n=0.30;
f0=0.002;                   % Initial void volume fraction
q1=1.5;                     % Some chosen Tvergaard fitting parameters
q2=1;
q3=q2^2;
k_omega=0:2:6;              % k_omega range and resolution
triAx=-1/3:.01:1;           % Triaxiality range and resolution
eps_p_max=10;               % Strain limit
d_eps_p=1e-3;               % Strain resolution
yFAccuracy=1e-6;            % Accuracy in yield function solving

% Preallocating variables
sigmaI(1)=0;
locuseps=zeros(size(k_omega),size(triAx));
locustA=zeros(size(k_omega),size(triAx));
locussigma_e=zeros(size(k_omega),size(triAx));
locusf=zeros(size(k_omega),size(triAx));

% Running main loop
for l=1:length(k_omega)
    % Clearing and preallocating variables
    locuscount=0;
    omega=zeros(size(triAx));
    for j=1:length(triAx)
        % Resetting variables
        eps_p=0:d_eps_p:eps_p_max;
        eps_M_p=zeros(size(eps_p));
        f=zeros(size(eps_p));
        f(1)=f0;
        sigma_M=zeros(size(eps_p));
        sigma_e=zeros(size(eps_p));
        dLambda=zeros(size(eps_p));
        locuscheck=0;

        for i=1:length(eps_p)
            sigma_M(i)=A+B*eps_M_p(i)^n;
            sigma_e(i)=sigma_M(i);
            yieldFunction=1;
            % Obtaining solution for sigma_e by using the Newton-Raphson
```

```
            % iterations to equate the yieldFunction to zero.
            while abs(yieldFunction)>yFAccuracy
                yieldFunction=(sigma_e(i)/sigma_M(i))^2+2*q1*f(i)* ...
                   cosh(3*q2*triAx(j)/2*sigma_e(i)/sigma_M(i))-1-f(i)^2*q3;
                yieldFunctionDerivative=2*sigma_e(i)/sigma_M(i)^2+2*q1* ...
                   f(i)*3*q2*triAx(j)/(2*sigma_M(i))*sinh(3*q2*triAx(j) ...
                   /2*sigma_e(i)/sigma_M(i));
                sigma_e(i) = sigma_e(i) - yieldFunction/ ...
                    yieldFunctionDerivative;
            end
            dLambda(i)=sigma_e(i)*d_eps_p/(2*(sigma_e(i)/sigma_M(i))^2+ ...
                3*f(i)*q1*q2*triAx(j)*sigma_e(i)/sigma_M(i)*sinh(3*q2*  ...
                triAx(j)/2*sigma_e(i)/sigma_M(i)));
            eps_M_p(i+1)=eps_M_p(i)+sigma_e(i)*d_eps_p/((1-f(i))*       ...
                sigma_M(i));
            % Calculating the value of the function omega for the current
            % triaxiality value
            if i==1
                if abs(triAx(j))<1/3
                    a=3;
                    b=-9*sigma_e(i)*triAx(j);
                    c=9*sigma_e(i)^2*triAx(j)^2-sigma_e(i)^2;
                    sigma1=(-b-sqrt(b^2-4*a*c))/(2*a);
                    sigma3=3*sigma_e(i)*triAx(j)-sigma1;
                    J3=2*sigma1^3/27-sigma1^2*sigma3/9-sigma1*sigma3^2/ ...
                        9+2*sigma3^3/27;
                    omega(j)=1-(27*J3/(2*sigma_e(i)^3))^2;
                    sigmaI(j)=sigma1;
                else
                    omega(j)=0;
                    sigmaI(j)=0;
                end
            end
            f(i+1)=f(i)+(1-f(i))*dLambda(i)*3*f(i)*q1*q2/sigma_M(i)*    ...
                sinh(3*q2*triAx(j)/2*sigma_e(i)/sigma_M(i))+k_omega(l)* ...
                f(i)*omega(j)*dLambda(i)*2*sigma_e(i)/sigma_M(i)^2;
            % Checking for localization and possibly set values of critical
            % quantities
            if i>1
                if sigma_e(i)<sigma_e(i-1)
                    locuscheck=1;
                    locuscount=locuscount+1;
                    locuseps(l,locuscount)=eps_p(i);
                    locuseps_M(locuscount)=eps_M_p(i);
                    locustA(l,locuscount)=triAx(j);
                    locussigma_e(l,locuscount)=sigma_e(i);
                    locusf(l,locuscount)=f(i);
                    plotlength=i;
                    break
                end
                end
        end
        if locuscheck==0
            plotlength=length(eps_p);
        end
    end
end
```

Appendix B
LS–DYNA material card for W460E penetraion simulation

```
*MAT_USER_DEFINED_MATERIAL_MODELS
$ Weldox 460E target
$1      MID        RO        MT       LMC       NHV    IORTHO     IBULK    ISHEAR
          1  7.85E+03        41        40        35         0        39        40
$2    IVECT     IFAIL    IHTERM    IHYPER      IEOS      LCMA
          1         1         0         0         0        40
$
$$$$$$$$$$$$$$$$$$$$$$$$$$$$$$$$$$$$$$$$$$$$$$$$$$$$$$$$$$$$$$$$$$$$$$$$$$$$$$$
$                                                                              $
$          DEFINE THE TWO FOLLOWING CARDS IF AND ONLY IF IORTHO = 1            $
$                                                                              $
$$$$$$$$$$$$$$$$$$$$$$$$$$$$$$$$$$$$$$$$$$$$$$$$$$$$$$$$$$$$$$$$$$$$$$$$$$$$$$$
$
$      AOPT      MAXC        XP        YP        ZP        A1        A2        A3
$         0         0         0         0         0         0         0
    0
$        V1        V2        V3        D1        D2        D3      BETA
$         0         0         0         0         0         0         0
$
$$$$$$$$$$$$$$$$$$$$$$$$$$$$$$$$$$$$$$$$$$$$$$$$$$$$$$$$$$$$$$$$$$$$$$$$$$$$$$$
$
$3         E        PR    IFLAG1    IFLAG2    IFLAG3        WC       PHI     GAMMA
 2.100E+11  0.330000         6         1         5         0         1         1
$4   SIGMA0    THETAR1       QR1    THETAR2       QR2   THETAR3       QR3         A
  4.1384+8  4.6781+9    2.20+8     3.95+8  4.9153+8         0         0         0
$
$$$$$$$$$             EXTENDED GURSON MODEL PARAMETERS                $$$$$$$$$$
$
$5       Q1        Q2        FN        PN        SN      KOMG        FC        FF
 1.5000000 1.0000000 0.0000000 0.0000000 1.0000000 5.5000000 0.1000000 0.3000000
$6       F0       FCR
    0.0001      0.01
$
$$$$$$$$$$$$$$$$$$$$$$$$$$$$$$$$$$$$$$$$$$$$$$$$$$$$$$$$$$$$$$$$$$$$$$$$$$$$$$$
$
$6        -         -    THETAX1       QX1    THETAX2       QX2      BULK     SHEAR
 0.0000000 0.0000000 0.0000000 0.0000000 0.0000000 0.0000000 2.059E+11 7.895E+10
$7   CSIGMA     PSIGMA     MSIGMA        CQ        PQ        MQ     ALPHA        ME
      0.01 5.00000-4          1 0.0000000 0.0000000 0.0000000  1.2000-5 0.0000000
$
$$$$$$$$$$        NB! SPECIFIC HEAT CT IS DEPENDENT ON LENGTH UNIT       $$$$$$$$$
$
$8         T         TO        TM        TC       RHO        CT    BETATQ
  293.0000  293.0000 1800.0000 1620.0000 7.85000+3 452.00000 0.9000000
$9        SO        QSA       ASA       BSA       CSA    DOTPSA      BETA       DCR
 0.0000000 0.0000000 0.0000000 0.0000000 0.0000000 0.0000000 0.0000000 0.0000000
$10     MW1       WCO       VO1     WCMIN     WCMAX       MW2       SCO       VO2
 0.0000000 0.0000000 0.0000000 0.0000000 0.0000000 0.0000000 0.0000000 0.0000000
$11   SCMIN     SCMAX   DELTATC      SOFT         -         -         -         -
 0.0000000 0.0000000 0.0000000 0.0000000 0.0000000 0.0000000 0.0000000 0.0000000
```